https://www.scirp.org/journal/ns Natural Science, 2022, Vol. 14, (No. 9), pp: 386-420

On the Solar Climate of the Moon and the Resulting Surface Temperature Distribution

Gerhard Kramm[1], Nicole Mölders[2], Martina Berger[3], Ralph Dlugi[3]

[1]Engineering Meteorology Consulting, Fairbanks, USA; [2]Department of Atmospheric Sciences and Geophysical Institute, University of Alaska Fairbanks, Fairbanks, USA; [3]Arbeitsgruppe Atmosphärische Prozesse (AGAP), Munich, Germany

Correspondence to: Gerhard Kramm, gerhard.kramm@hotmail.com

Keywords: Solar Climate, Temperature Inequality, Hölder's Inequility, Global Radiation Budget, Local Radiation Budget, Global Energy Budget, Local Energy Budget, Global Albedo, Global Averaging, Effective Radiation Temperature, Surface Temperature, Slab Temperature, Multilayer-Force-Restore Method

Received: August 19, 2022 **Accepted:** September 27, 2022 **Published:** September 30, 2022

ABSTRACT

The solar climate of our Moon is analyzed using the results of numerical simulations and the recently released data of the Diviner Lunar Radiometer Experiment (DLRE) to assess (a) the resulting distribution of the surface temperature, (b) the related global mean surface temperature $\langle T_s \rangle$, and (c) the effective radiation temperature T_e often considered as a proxy for $\langle T_s \rangle$ of rocky planets and/or their natural satellites, where T_e is based on the global radiation budget of the well-known "thought model" of the Earth in the absence of its atmosphere. Because the Moon consists of similar rocky material like the Earth, it comes close to this thought model. However, the Moon's astronomical features (e.g., obliquity, angular velocity of rotation, position relative to the disc of the solar system) differ from that of the Earth. Being tidally locked to the Earth, the Moon's orbit around the Sun shows additional variation as compared to the Earth's orbit. Since the astronomical parameters affect the solar climate, we predicted the Moon's orbit coordinates both relative to the Sun and the Earth for a period of 20 lunations starting May 24, 2009, 00:00 UT1 with the planetary and lunar ephemeris DE430 of the Jet Propulsion Laboratory of the California Institute of Technology. The results revealed a mean heliocentric distance for the Moon and Earth of 1.00124279 AU and 1.00166376 AU, respectively. The mean geocentric distance of the Moon was 384792 km. The synodic and draconic months deviated from their respective means in a range of −5.7 h to 6.9 h and ±3.4 h, respectively. The deviations of the anomalistic months from their mean range between −2.83 d and 0.97 d with the largest negative deviations occurring around the points of inflection in the curve that represents the departure of the

synodic month from its mean. Based on the two successive passages of the Sun through the ascending node of the lunar equator plane, the time interval between them corresponds to 347.29 days, *i.e.*, it is slightly longer than the mean draconic year of 346.62 days. We computed the local solar insolation as input to the multilayer-force restore method of Kramm *et al.* (2017) that is based on the local energy budget equation. Due to the need to spin up the distribution of the regolith temperature to equilibrium, analysis of the model results covers only the last 12 lunations starting January 15, 2010, 07:11 UT1. The predicted slab temperatures, T_{slab}, considered as the realistic surface temperatures, follow the bolometric temperatures, T_{bol}, acceptably. According to all 24 DLRE datasets related to the subsolar longitude ϕ_{ss}, the global averages of the bolometric temperature amounts to $\langle T_{bol} \rangle = 201.1\ \mathrm{K} \pm 0.6\ \mathrm{K}$. Based on the globally averaged emitted infrared radiation of $\langle F_{IR} \rangle = 290.5\ \mathrm{W \cdot m^{-2}} \pm 3.0\ \mathrm{W \cdot m^{-2}}$ derived from the 24 DLRE datasets, the effective radiative temperature of the Moon is $T_{e,M} = \langle T_{bol}^4 \rangle^{1/4} = 271.0\ \mathrm{K} \pm 0.7\ \mathrm{K}$ so that $\langle T_{bol} \rangle \cong 0.742 T_{e,M}$. These empirical results confirm Kramm *et al.*'s theoretical results for the Moon of $\langle T_{slab} \rangle \cong 197.9\ \mathrm{K}$, $T_{e,M} \cong 266.4\ \mathrm{K}$, and $\langle T_{slab} \rangle \cong 0.743 T_{e,M}$. The DLRE observations suggest that in the case of rocky planets and their natural satellites, the globally averaged surface temperature is notably lower than the effective radiation temperature. They differ by a factor that depends on the astronomical parameters especially on the angular velocity of rotation.

1. INTRODUCTION

According to von Hann [1, 2], the notion "solar climate" to which, for instance, Ptolemy's climatic zones are related is based on the thought model of an Earth in the absence of its atmosphere. Von Hann stated [2]:

> "If the surface of the Earth were occupied altogether by land, and if there were no surrounding atmosphere, the condition of our planet would be somewhat similar to that of the Moon at the present time. Under these conditions, the distribution of temperature over the Earth would depend solely upon the amount of heat received from the sun at any given place, and upon the loss of heat by radiation at that place. As these two factors would necessarily be the same at all points along the same parallel of latitude, the zones of equal temperature would coincide with the parallels of latitude. Even the presence of a vaporless atmosphere would interfere but little with this distribution of temperature, for only the absolute amounts of heat received at, and radiated from, the surface of the earth would thereby be affected. It is true that convectional currents would be produced under these conditions; but as there would be no reason for the more frequent occurrence of warm or cold air currents along some meridians than others, the distribution of temperature in zones bounded by the parallels of latitude would not thereby be interfered with."

Thus, the solar climate (also called the mathematical climate [1, 2]) of the Earth and its Moon essentially depends on astronomic conditions like the heliocentric distance, the obliquity of rotation axis with respect to the normal of the ecliptic plane, the angular velocity of the rotation, and the total solar irradiance (TSI), if scaled to 1 AU customarily called the solar constant. With respect to geological time scales, also changes in the precession of Earth's rotation axis, and long-term variations of the eccentricity, obliquity, and precession of the Perihelion caused by the Sun, Moon and planets of our solar system must be addressed [3-9]. In the case of the Moon, the precession of the perigee as well as the precession of the lunar orbit's longitude of the ascending node must be taken into account, which have periods of 8.85 years and

18.6 years, respectively.

The formula for the effective radiation temperature, T_e, either of the Earth (with or without an atmosphere) or the Moon (or any other planet and natural satellites),

$$T_e = \left(\frac{(1-\alpha_G)S}{4\varepsilon_G \sigma} \right)^{\frac{1}{4}} \tag{1.1}$$

is crudely based on the solar climate. This formula is based on a global radiative equilibrium which means that the infrared radiation emanating from this conceptual Earth, $\varepsilon_G \sigma T_e^4$, is equal to the globally averaged absorbed solar radiation, $(1-\alpha_G)S/4$ [10]. Here, α_G is the global (or planetary) albedo in the solar range, S is the solar constant, ε_G is the global emissivity, and $\sigma = 5.67 \times 10^{-8}\ \mathrm{W \cdot m^{-2} \cdot K^{-4}}$ is Stefan's constant. Note that the power law of Stefan [11] and Boltzmann [12] is only valid on a local scale. Applying it on a global scale notably disagrees with the prerequisites and assumptions on which the derivation of this power law is based. In the case of the Earth, the solar constant is about $S = 1361\ \mathrm{W \cdot m^{-2}}$ [13-16]. With the usual assumptions of $\alpha_G = 0.30$ and $\varepsilon_G = 1.0$, one obtains $T_e \approx 255\ \mathrm{K} = -18^{\circ}\mathrm{C}$. Thus, the so-called natural atmospheric greenhouse effect is usually quantified by $\Delta T = \langle T_{ns} \rangle - T_e \approx 33\ \mathrm{K}$, where $\langle T_{ns} \rangle \approx 288\ \mathrm{K}$ (e.g., [2, 17-26]) is the globally averaged near-surface air temperature. Here, the angle brackets, $\langle \ldots \rangle$, define the global average (e.g., [19, 27-29])

$$\langle \psi \rangle = \frac{1}{4\pi} \int_0^{2\pi} \int_0^{\pi} \psi(\theta,\varphi) \sin\theta \,\mathrm{d}\theta \,\mathrm{d}\varphi = \frac{1}{2} \int_0^{\pi} \bar{\psi}(\theta) \sin\theta \,\mathrm{d}\theta \tag{1.2}$$

with the zonal average (e.g., [28-32]),

$$\bar{\psi}(\theta) = \frac{1}{2\pi} \int_0^{2\pi} \psi(\theta,\varphi) \,\mathrm{d}\varphi \tag{1.3}$$

where $\psi(\theta,\varphi)$ is a field quantity like the solar insolation, $F_S(\theta,\varphi)$, the absorbed solar irradiance, $Q(\theta,\varphi)$, the infrared irradiance, $F_{IR}(\theta,\varphi)$, and the surface temperature, $T_s(\theta,\varphi)$.

The assumption of a global albedo of about $\alpha_G = 0.30$, however, is far from reality because this value is related to the entire Earth-atmosphere system. For $\alpha_G = 0.30$, the infrared radiation emitted to space would be that at the top of the atmosphere (TOA) of about $\langle F_{IR} \rangle \cong 238.2\ \mathrm{W \cdot m^{-2}}$. The cloud cover primarily contributes to this value of the global albedo, but a cloud cover cannot exist in the thought model of the Earth in the absence of its atmosphere. Furthermore, the global emissivity of such a conceptual Earth is unknown. Both quantities might be related to those of the Earth's Moon, as done by Kramm *et al.* [29].

Since, however, the thought model of an Earth in the absence of an atmosphere eludes observation, there are some assumptions that can be combined at will. Inserting, for instance, $\varepsilon_G = 0.8$ as assumed by Schack [33], and $\alpha_G = 0.07$ as suggested by Budyko [34] for the Earth in the absence of its atmosphere into Equation (1.1) would provide $T_e = 289\ \mathrm{K}$. Thus, we would obtain $\Delta T = \langle T_{ns} \rangle - T_e \approx -1\ \mathrm{K}$.

The effective radiation temperature of the Earth either with or without an atmosphere is only a synonym for the global average of the infrared radiation emitted to space. It is a measure of the intensity of the radiation emanating from the Earth and, therefore, says nothing about the existing temperature distribution [35]. It was considered, for instance, by Defant and Obst [36], Lenard [37], Möller [38], and later adopted by many others like Hansen *et al.* [24] to quantify the so-called greenhouse effect. However, in the case of the Earth in the absence of its atmosphere, T_e would only correspond to a globally averaged surface temperature if the surface temperature were uniformly distributed, which is, by far, not the case. A uniform distribution of the surface temperature would only exist in the trivial case that the solar constant for the planet or natural satellite would be zero. As illustrated in **Figures 1-3**, the distribution of the surface temperature on a planet or a natural satellite (like Earth's Moon or Jupiter's Galilean moon Io) in the absence of an atmosphere is non-uniform. As outlined by von Hann, this distribution of the surface temperature is mainly governed by the solar insolation defined as the flux of solar radiation per unit of horizontal area for a given location [8].

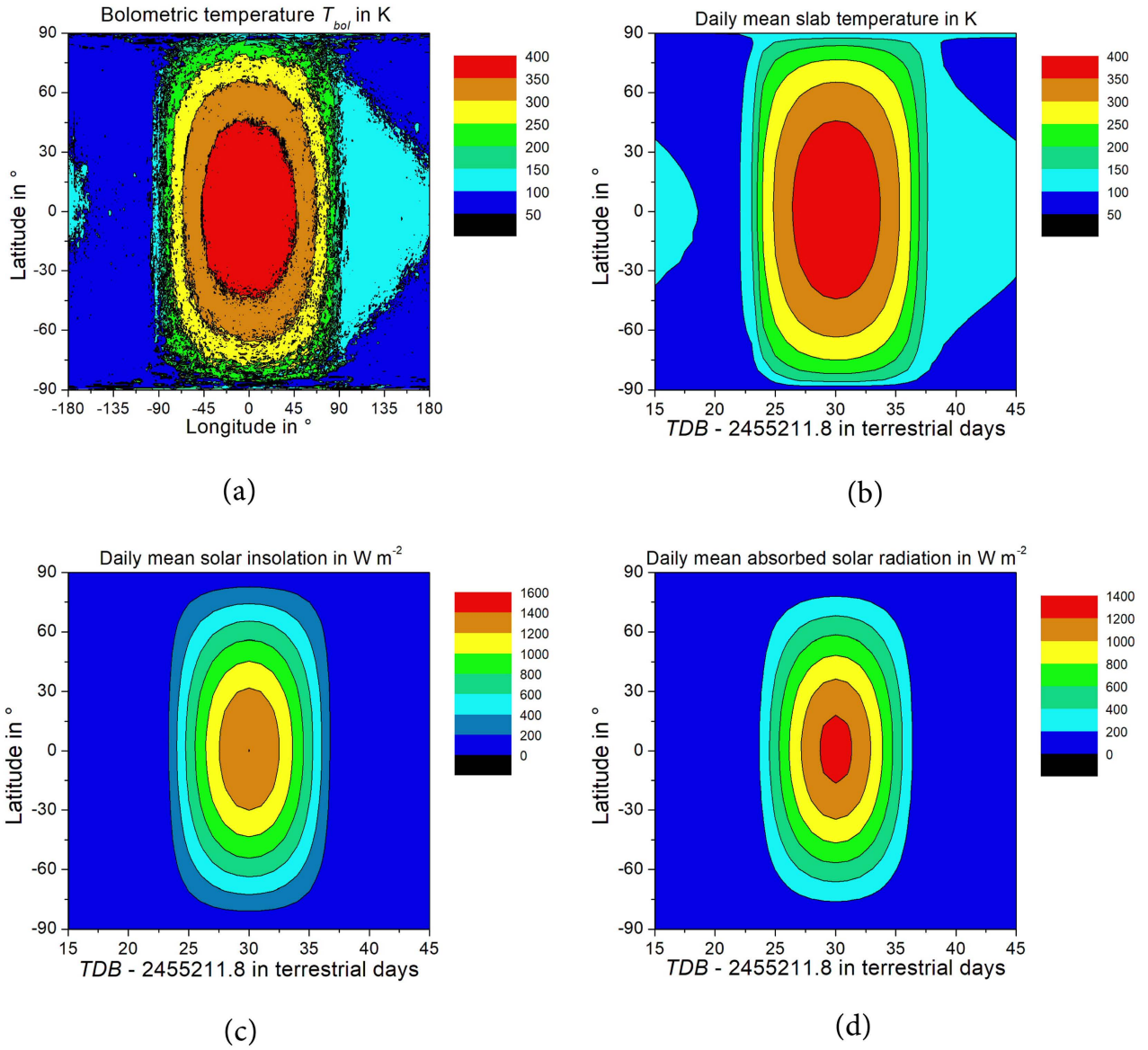

Figure 1. Distributions of (a) the bolometric temperature obtained from the Lunar Reconnaissance Orbiter Diviner Lunar Radiometer Experiment for the subsolar longitude $\phi_{ss} = 0^{\circ}\mathrm{E}$ according to Williams *et al.*, [39], and the daily mean values of (b) the slab temperature, (c) the solar insolation at Moon's surface, and (d) the absorbed solar radiation calculated for twelve synodic months starting with TDB = 2455211.8 (January 15, 2010, 11:07 UT1, New Moon) and the latitudes ranging from $\phi = 90^{\circ}$ (North Pole) to $\phi = -90^{\circ}$ (South Pole) at an equidistant distance of $\Delta\phi = 5^{\circ}$, where 144 values per day were used for daily averaging. The numerical simulations were performed using the multilayer-force-restore method that is based on Equation (2.1) and a multilayer numerical model that is based on Equation (2.6) for calculating the heat transfer in the regolith (adopted from Kramm *et al.* [29]).

Note that the notion "terrestrial day" used in **Figure 1** means the length of the day of 86,400 s = 24 h. It is about 236 s longer than the Earth's sidereal rotation period. Hereafter, we only use "day" (d), where 365.25 d = 1 Julian year.

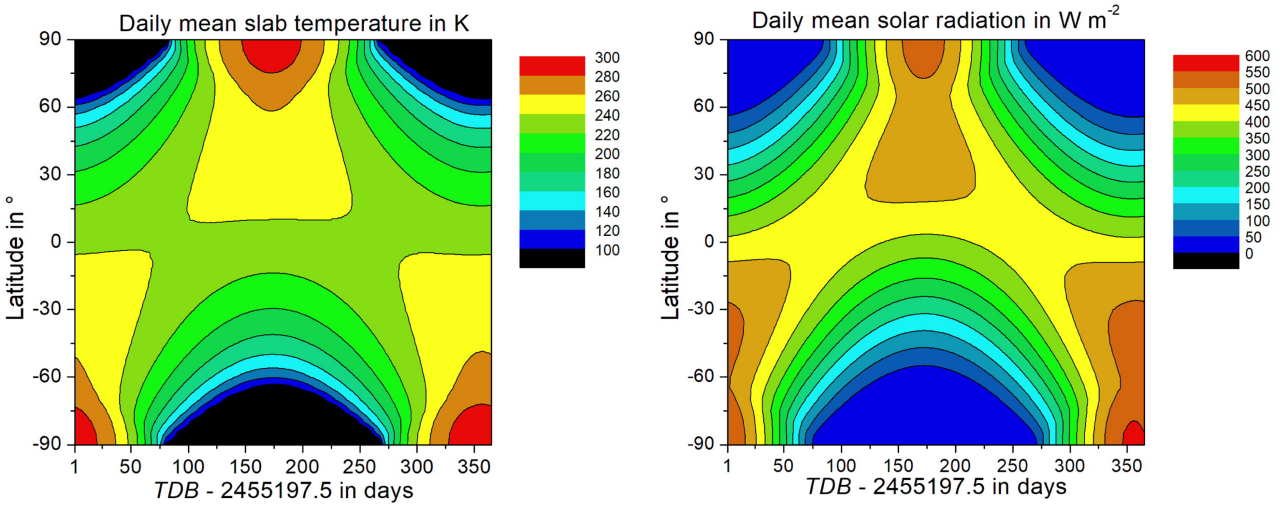

(a) (b)

Figure 2. Daily mean values of (a) the slab temperature according to Equation (2.1), and (b) the solar insolation at the surface of the Earth in the absence of the atmosphere which were calculated for all days of a year, starting with TDB = 2455197.5 (January 1, 2010, 00:00 UT1) and the latitudes ranging from $\phi = 90^\circ$ (North Pole) to $\phi = -90^\circ$ (South Pole) at an equidistant distance of $\Delta\phi = 5^\circ$, where 144 values per day were used for daily averaging. The numerical simulations were performed using the so-called multilayer-force-restore method as well (adopted from Kramm *et al.* [29]).

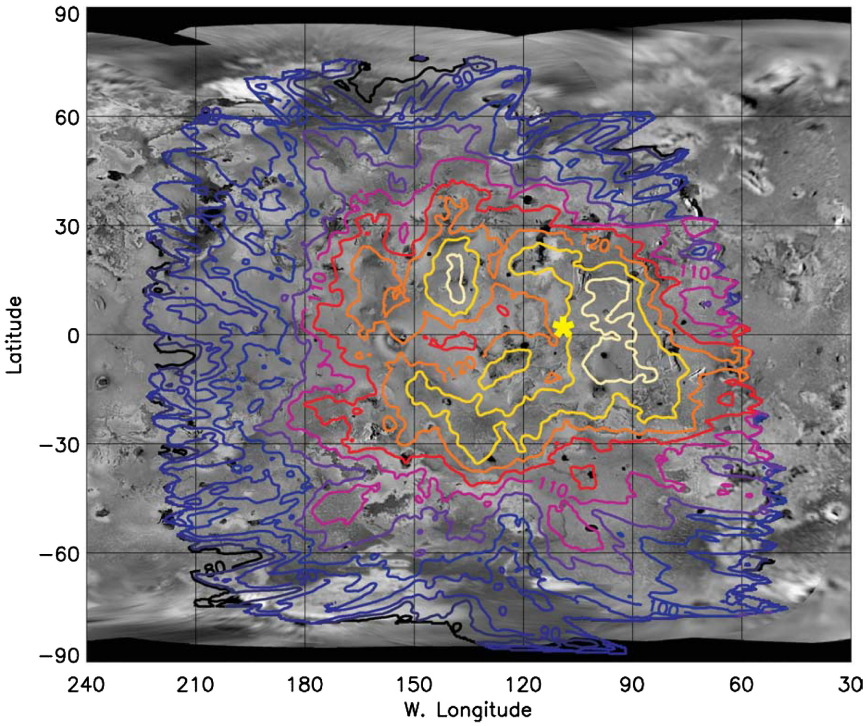

Figure 3. Map of daytime brightness temperature in the PPR 27 μm filter, superimposed on an SSI map of Jupiter's Galilean moon Io, from the 31IPDGTM_01 observation. Contour interval is 5 K. Approximate location of the sub-solar point is marked with an * (adopted from Rathbun *et al.* [51]).

The concept of effective radiation temperature was originally developed for stars like our Sun (e.g., [35, 40-42]). It seems that this concept is unsuitable for planets and their natural satellites. The solar irradiance, *F*, reaching the TOA or—if an atmosphere plays no role—the surface of either a planet or a natural satellite in our solar system at the sub-solar point is given by

$$F = \left(\frac{r_{Sun}}{r}\right)^2 F_{Sun} \tag{1.4}$$

where F_{Sun} is the solar emittance [8, 9, 43, 44], $r_{Sun} \cong 6.963\times10^5$ km [45] is the visible radius of the Sun, and r is the actual heliocentric distance of either the planet or the natural satellite. Formula (1.4) is based on the fact that the radiant power emitted by the Sun is kept constant when the solar radiation is propagating through the space because of energy conservation principles in the absence of an intervening medium [8, 46, 47]. This radiant power (also called the luminosity) is given by

$$L = 4\pi r_{Sun}^2 F_{Sun} = 4\pi r^2 F = 3.828\times10^{26}\ \text{W} \tag{1.5}$$

Inserting the mean heliocentric distance, r_0, of a planet or a natural satellite into Equation (1.4) provides the respective solar constant

$$S = \left(\frac{r_{Sun}}{r_0}\right)^2 F_{Sun} \tag{1.6}$$

Combining formulae (1.4) and (1.6) yields

$$F = \left(\frac{r_0}{r}\right)^2 S \tag{1.7}$$

The solar constant of the Earth of $S \cong 1361\ \text{W}\cdot\text{m}^{-2}$ mentioned before is related to the mean heliocentric distance of $r_0 \cong 1.496\times10^8$ km (nearly 1 AU) [14, 48-50], where the actual heliocentric distance of the Earth (strictly spoken the Earth-Moon barycenter, EMB) ranges from $r \cong 1.471\times10^8$ km at the Perihelion to $r \cong 1.521\times10^8$ km at the Aphelion.

Inserting Equation (1.6) into Equation (1.1) provides

$$T_e = \left(\frac{(1-\alpha_G)F_{Sun}}{\varepsilon_G\sigma}\right)^{\frac{1}{4}}\left(\frac{r_{Sun}}{2r_0}\right)^{\frac{1}{2}} = \left(\frac{F_{Sun}}{\sigma}\right)^{\frac{1}{4}}\left(\frac{1-\alpha_G}{\varepsilon_G}\right)^{\frac{1}{4}}\left(\frac{r_{Sun}}{2r_0}\right)^{\frac{1}{2}} \tag{1.8}$$

Introducing the effective radiation temperature of the Sun, $T_{Sun} = (F_{Sun}/\sigma)^{1/4}$ [41], assuming $\varepsilon_G = 1$ and replacing r_0 by the orbital semi-major axis, *a* yield [52]

$$T_e \cong T_{Sun}(1-\alpha_G)^{\frac{1}{4}}\left(\frac{r_{Sun}}{2a}\right)^{\frac{1}{2}} \tag{1.9}$$

The formula should also serve for determining the effective radiation temperature of Earth analogs. Furthermore, the luminosity (Equation (1.5)) is used to define the scaled semi-majsor axis by [52]

$$a_s = \frac{a}{\sqrt{L}} = (4\pi S)^{-\frac{1}{2}} \tag{1.10}$$

Unfortunately, the effective radiation temperature is not unambiguous because non-uniform distributions of the surface temperature are also compatible with the global radiation balance. Gerlich and Tscheuschner [53], for instance, derived the following formula for the globally averaged surface temperature of a radiation-exposed static globe in the absence of its atmosphere:

$$\langle T_s \rangle = \frac{2^{3/2}}{5} T_e \cong 0.566 T_e \tag{1.11}$$

As assumed by these authors, $T_s(\theta,\varphi)$ is the surface temperature that is based on the local radiation balance given by

$$\left(1-\alpha\left(\Theta_0,\theta,\varphi\right)\right)F\cos\Theta_0=\varepsilon\left(\theta,\varphi\right)\sigma T_s^4\left(\theta,\varphi\right) \tag{1.12}$$

where $Q=\left(1-\alpha\left(\Theta_0,\theta,\varphi\right)\right)F\cos\Theta_0$ is the absorbed solar radiation, $\alpha\left(\Theta_0,\theta,\varphi\right)$ is the integral albedo of the solar range, Θ_0 is the local zenith distance of the Sun's center, and the infrared radiation emitted by the regolith in the close vicinity of the surface is given by the power law of Stefan and Boltzmann $F_{IR}=\varepsilon\left(\theta,\varphi\right)\sigma T_s^4\left(\theta,\varphi\right)$, where $\varepsilon\left(\theta,\varphi\right)$ is the integral relative emissivity and σ is Stefan's constant. As both the Earth and the Moon are considered as spheres, the location is simply characterized by the zenith and azimuthal angles θ and φ, respectively. The zenith angle, θ, ranges from 0 (North Pole) to π (South Pole), and the azimuthal angle, φ, ranges from 0 to 2π. The global average of the absorbed solar radiation is given by

$$\left\langle Q\right\rangle=\left\langle F\cos\Theta_0\right\rangle-\left\langle\alpha\left(\Theta_0,\theta,\varphi\right)F\cos\Theta_0\right\rangle=\left(1-\alpha_G\right)\left\langle F\cos\Theta_0\right\rangle \tag{1.13}$$

where

$$\alpha_G=\frac{\left\langle\alpha\left(\Theta_0,\theta,\varphi\right)F\cos\Theta_0\right\rangle}{\left\langle F\cos\Theta_0\right\rangle} \tag{1.14}$$

defines the globally averaged albedo in the solar range. Generally, $\alpha_G\neq\left\langle\alpha\left(\Theta_0,\theta,\varphi\right)\right\rangle$, except for $\alpha\left(\Theta_0,\theta,\varphi\right)=const$. Note that $\left\langle F\cos\Theta_0\right\rangle\cong S/4$. The global average of the emitted infrared radiation is given by

$$\left\langle F_{IR}\right\rangle=\left\langle\varepsilon\left(\theta,\varphi\right)\sigma T_s^4\left(\theta,\varphi\right)\right\rangle=\varepsilon_G\sigma\left\langle T_s^4\left(\theta,\varphi\right)\right\rangle \tag{1.15}$$

where

$$\varepsilon_G=\frac{\left\langle\varepsilon\left(\theta,\varphi\right)T_s^4\left(\theta,\varphi\right)\right\rangle}{\left\langle T_s^4\left(\theta,\varphi\right)\right\rangle} \tag{1.16}$$

defines the globally averaged emissivity, where $\varepsilon_G\neq\left\langle\varepsilon\left(\theta,\varphi\right)\right\rangle$, except for $\varepsilon\left(\theta,\varphi\right)=const$.

Choosing $\alpha_G=0.30$, and $\varepsilon_G=1.0$, as done for instance by Gerlich and Tscheuschner [53], provides $\left\langle T_s\right\rangle\cong 144.3\text{ K}$. Even though this global average of the surface temperature drastically differs from effective radiation temperature, the globally averaged emitted infrared radiation is $\left\langle Q\right\rangle=\left\langle F_{IR}\right\rangle=\sigma\left\langle T_s^4\left(\theta,\varphi\right)\right\rangle\cong 238\text{ W}\cdot\text{m}^{-2}$. They denoted $\left\langle T_s\right\rangle$ as the "physical temperature." This notion, however, is infelicitous. As a global average, $\left\langle T_s\right\rangle$ has no physical meaning. Its sole purpose is to compare it with $\left\langle T_{ns}\right\rangle$ because both quantities are globally averaged in the same manner. With respect to their results, Gerlich and Tscheuschner argued that the average temperatures are considerably lower than the absolute temperature's fourth root of the averaged fourth power expressed by their temperature inequality [53]

$$\left\langle T_s\right\rangle\leq\sqrt[4]{\left\langle T_s^4\right\rangle}, \tag{1.17}$$

verified by them with the aid of Hölder's [54] inequality, but formulated for integrals [55].

Kramm *et al.* [29] obtained $\left\langle T_s\right\rangle\cong 148.4\text{ K}$, $\left\langle Q\right\rangle\cong 279.7\text{ W}\cdot\text{m}^{-2}$, and $\left\langle F_{IR}\right\rangle\cong 279.6\text{ W}\cdot\text{m}^{-2}$ for an obliquely rotating Earth in the absence of its atmosphere when using Equation (1.12), $\varepsilon\left(\theta,\varphi\right)=0.98$, and Keihm's [56] empirical formula rearranged to

$$\alpha\left(\Theta_0\right)=\alpha_0+\left(\frac{\Theta_0}{45^\circ}\right)^3\left(a+b\left(\frac{\Theta_0}{45^\circ}\right)^5\right) \tag{1.18}$$

where $\alpha_0=0.10$ is the normal albedo, $a=0.045$ and $b=5.47\times10^{-4}$ are empirical parameters (with exception of *b*, all other values are from observations of the Diviner Lunar Radiometer Experiment

(DLRE) [57, 58] aboard NASA's Lunar Reconnaissance Orbiter (LRO) [59-61]). Because $\alpha_G = 0.178$, the effective radiation temperature is $T_e \cong 266.4\,\mathrm{K}$. This means that the result of Gerlich and Tscheuschner [53] for a non-rotating Earth in the absence of its atmosphere holds even for an obliquely rotating globe if atmospheric effects were negligible.

Equation (1.12) expresses the solar climate in its historical sense, *i.e.*, the distribution of temperature over the Earth in the absence of its atmosphere would depend solely upon the amount of heat received from the Sun at any given place, and upon the loss of heat by radiation at that place [1, 2]. However, as already demonstrated by Wesselink [62] in the case of the Moon, the local radiation balance fails completely during the nighttime because it would provide $T_s = 0\,\mathrm{K}$. It is therefore essential to expand the concept of solar climate in such a way that such a model artifact is generally excluded. Consequently, the soil heat flux has to be considered as well, as done, for instance, by Wesselink [62], Jaeger [63], Cremers *et al.* [64], Mitchell and de Pater [65], Vasavada *et al.* [58, 66], Bauch *et al.* [67, 68], Hu *et al.* [69], and Kramm *et al.* [29].

An Earth in the absence of an atmosphere, however, is beyond the scope of observation. Consequently, at least, the plausibility of this thought model must be assessed in another way. In our solar system, for instance, the planet Mercury and our Moon are suitable approximations for a rocky planet without an atmosphere because the densities of their atmospheres are very low. Therefore, these Earth analogs come very close to the thought model of an Earth in the absence of its atmosphere. However, their astrometric features considerably differ from those of the Earth.

The Earth's period of rotation is 23.9345 hours, which corresponds to an angular velocity of rotation of $\omega_E \cong 7.292\times10^{-5}\,\mathrm{s}^{-1}$. Since the sidereal period of rotation of the Moon is 655.73 hours, which corresponds to an angular velocity of $\omega_{Mo} \cong 2.662\times10^{-6}\,\mathrm{s}^{-1}$, the Moon rotates 27.4 times slower than the Earth. Mercury's sidereal period of rotation is 1407.6 hours and consequently the angular velocity of its rotation is $\omega_{Me} \cong 1.240\times10^{-6}\,\mathrm{s}^{-1}$. This means that Mercury rotates 58.8 times slower than the Earth and 2.15 times slower than the Moon.

The mean heliocentric distance of Mercury is only $r_{0,Me} \approx a_{Me} = 5.791\times10^{7}\,\mathrm{km} = 0.3871\,\mathrm{AU}$ leading to a solar constant of

$$S_{Me} = \left(\frac{r_{0,E}}{r_{0,Me}}\right)^2 S \cong 9083\,\mathrm{W\cdot m^{-2}} \tag{1.19}$$

In addition, Mercury's orbit shows an extremely high eccentricity of $e_{Me} \cong 0.2056$, while that of the Earth orbit is only $e_E \cong 0.0167$. Since Mercury's heliocentric distance ranges between 4.600×10^7 km (Perihelion) and 6.982×10^7 km (Aphelion), its total solar irradiance (TSI) varies from $F_{Me} \approx 14395\,\mathrm{W\cdot m^{-2}}$ at Perihelion to $F_{Me} \approx 6249\,\mathrm{W\cdot m^{-2}}$ at Aphelion. A special feature of Mercury is that the angular velocity of the orbit near the Perihelion slightly exceeds that of the rotation, which leads to a secondary sunrise (e.g., [66, 68, 70, 71]). Against this background, the Moon is preferable for testing the plausibility of the thought model of an Earth in absence of its atmosphere. Further reasons are the existence of (a) the in-situ temperature measurements carried out with the help of thermocouples as part of the heat flow experiments of the Apollo Lunar Surface Experiment Package (ALSEP) at the Apollo 15 landing site Hadley Rille/Apennine Mountains [72] and the Apollo 17 landing site Taurus-Littrow [73] and (b) the bolometric temperatures provided by the DLRE [57], available to us since April 2018. Nonetheless, the Mercury Radiometer and Thermal Infrared Spectrometer (MERTIS) that is part of the BepiColombo Mission launched in October 2018 [68, 74] may provide a reliable database for evaluating model results regarding Mercury's solar climate.

Kramm *et al.* [29] used their multilayer-force-restore method to compute the global average of the Moon's surface temperature and in a further step that of the Earth in the absence of its atmosphere. Kramm *et al.* obtained for the Moon $\langle T_{slab}\rangle \cong 197.9\,\mathrm{K}$ and for the Earth in the absence of its atmosphere $\langle T_{slab}\rangle \cong 220.7\,\mathrm{K}$. Thus, the outcome notably differs. This difference can be explained by the 27.4 times higher angular velocity of the Earth compared to that of the Moon, *i.e.*, the response time of the emitted

infrared radiation with respect to the absorbed solar radiation causes different effects [29]. Kramm *et al.* obtained for the Moon $\left\langle T_{slab}^4(\theta,\varphi)\right\rangle^{1/4} \cong 266.4\,\mathrm{K}$ and for the Earth $\left\langle T_{slab}^4(\theta,\varphi)\right\rangle^{1/4} \cong 266.5\,\mathrm{K}$, *i.e.*, $\left\langle T_{slab}^4(\theta,\varphi)\right\rangle^{1/4}$ and T_e substantially agree with each other, but in contrast to Equation (1.11), $\langle T_{slab}\rangle \cong 0.743\left\langle T_{slab}^4(\theta,\varphi)\right\rangle^{1/4}$ is valid for the obliquely rotating Moon and $\langle T_{slab}\rangle \cong 0.828\left\langle T_{slab}^4(\theta,\varphi)\right\rangle^{1/4}$ for the obliquely rotating Earth in the absence of its atmosphere. These results confirm the temperature inequality of Gerlich and Tscheuschner [53].

Kramm *et al.* [29] preliminarily validated their model results obtained for the Moon by comparing the zonal mean bolometric temperatures of the DLRE published by Williams *et al.* [39] for numerous parallels of latitude. As mentioned before, these DLRE datasets are meanwhile available. The goals of our paper are, therefore, (a) to expand the notion "solar climate" to predict the related distribution of the surface temperature in a realistic manner, (b) to evaluate the model results of Kramm *et al.* on the basis of the 24 DRLE datasets, (c) to compare the globally averaged surface temperature with the effective radiation temperature, and (d) to assess the temperature inequality of Gerlich and Tscheuschner [53] in the case of Earth analogs, where we exemplarily consider our Moon as a test bed.

2. THE NUMERICAL MODEL FOR THE MOON REGOLITH

Since the soil heat flux has to be considered in deriving the surface temperature [53], Kramm *et al.* [29] derived the following local energy budget equation for a thin slab of the regolith adjacent to the surface of either the Moon or the Earth in the absence of its atmosphere:

$$\vartheta\frac{\mathrm{d}}{\mathrm{d}t}\left\langle c\rho T_{slab}\right\rangle_V = \left(1-\alpha\left(\Theta_0,\theta,\varphi\right)\right)F\cos\Theta_0 - \varepsilon(\theta,\varphi)\sigma T_{slab}^4(\theta,\varphi) - H_{sl}(\theta,\varphi) \tag{2.1}$$

Here, t is time, T_{slab}, ρ, and c, are the temperature, bulk density, and specific heat of this slab, respectively. The soil volume average is defined by

$$\left\langle c\rho T_{slab}\right\rangle_V = \frac{1}{V_{slab}}\int_{V_{slab}} c\rho T_{slab}\mathrm{d}V \tag{2.2}$$

The volume V_{slab} is given by $V_{slab} = C_{slab}\vartheta$, where C_{slab} is the cross section, and $\vartheta = 2\,\mathrm{cm}$ is the thickness of this slab. Thus, the temperature T_{slab} represents the temperature of the slab adjacent to the surface. Assuming that T_{slab}, ρ, and c are homogeneously distributed in this thin layer leads to

$$R_t\frac{\mathrm{d}T_{slab}}{\mathrm{d}t} = \left(1-\alpha\left(\Theta_0,\theta,\varphi\right)\right)F\cos\Theta_0 - \varepsilon(\theta,\varphi)\sigma T_{slab}^4(\theta,\varphi) - H_{sl}(\theta,\varphi) \tag{2.3}$$

where $R_t = c\rho\vartheta$ is the thermal inertial coefficient. Furthermore, $H_{sl}(\theta,\varphi)$ is the vertical component of the soil heat flux density expressed by the one-dimensional form of Fourier's law of heat conduction (e.g., [62-66, 75-77]),

$$H_{sl}(\theta,\varphi) = -k_h(\theta,\varphi)\left.\frac{\partial T_{sl}}{\partial z}\right|_{\theta,\varphi} \tag{2.4}$$

Here, T_{sl} is the soil temperature, and $k_h(\theta,\varphi)$ is the thermal conductivity. The soil heat flux density characterizes the exchange of the slab with soil layers below. Henceforth, a flux density is called a flux for ease of readability. The difference between the absorbed solar radiation and the emitted infrared radiation mainly governs the direction of $H_{sl}(\theta,\varphi)$.

Under steady-state conditions, the left-hand side of Equation (2.3) is zero leading to

$$\left(1-\alpha\left(\Theta_0,\theta,\varphi\right)\right)F\cos\Theta_0 - \varepsilon(\theta,\varphi)\sigma T_s^4(\theta,\varphi) - H_{sl}(\theta,\varphi) = 0 \tag{2.5}$$

This means that the slab, characterized by T_{slab}, ρ, c, and ϑ, no longer occurs, and T_{slab} is re-

placed by the "surface temperature" T_s. Wesselink [62], Jaeger [63], Cremers *et al.* [64], Mitchell and de Pater [65], Vasavada *et al.* [58, 66], Bauch *et al.* [67, 68], for instance, used Equation (2.5) together with Equation (2.4) to compute the surface temperature for various areas on the Moon.

Kramm *et al.* [29] used Equation (2.3) together with Equation (2.4) to predict the distributions of slab temperatures for both the Earth's Moon and the Earth in the absence of its atmosphere. A numerical multilayer model for the regolith based on

$$\rho c \frac{\partial T_{sl}}{\partial t} = \frac{\partial}{\partial z}\left(k_h \frac{\partial T_{sl}}{\partial z} \right) \tag{2.6}$$

was used to predict the both the temperature and the heat flux in the layer of the regolith below the slab. Kramm *et al.* used 16 levels in their computations and a maximum depth of z_r = 3.20 m, at which $T_{sl,r}$, is considered as time-invariant, but dependent on latitude [66].

For the bulk density and the thermal conductivity, Kramm *et al.* considered the formulae of Vasavada *et al.* [58],

$$\rho(z) = \rho_b - (\rho_b - \rho_t)\exp\left(-\frac{z}{0.06} \right) \tag{2.7}$$

where $\rho_t = 1300\ \mathrm{kg \cdot m^{-3}}$ and $\rho_b = 1800\ \mathrm{kg \cdot m^{-3}}$ are the bulk densities close to the surface and at the depth z_r, respectively, and

$$k_h(z,T) = k_{h,b} - (k_{h,b} - k_{h,t})\exp\left(-\frac{z}{0.06} \right) + k_{h,t}\chi\left(\frac{T}{T_{350}} \right)^3 \tag{2.8}$$

with $k_{h,t} = 6.0 \times 10^{-4}\ \mathrm{W \cdot m^{-1} \cdot K^{-1}}$, $k_{h,b} = 7.0 \times 10^{-3}\ \mathrm{W \cdot m^{-1} \cdot K^{-1}}$, and $\chi = 2.7$. The heat capacity was calculated by

$$c = \begin{cases} -23.17 + 744.5\left(\frac{T}{T_{350}} \right) + 1839\left(\frac{T}{T_{350}} \right)^2 - 3160\left(\frac{T}{T_{350}} \right)^3 + 1449\left(\frac{T}{T_{350}} \right)^4 & \text{for } T \le T_{350} \\ 1009 - 5307\exp\left(-3.5\left(\frac{T}{T_{350}} \right) \right) & \text{for } T > T_{350} \end{cases} \tag{2.9}$$

The formula for $T \le T_{350}$ is based on the analysis of lunar soils samples from the lunar landing sites Fra Mauro (Apollo 14), Hadley-Apeninne Base (Apollo 15), and Descartes Highlands (Apollo 16) by Hemingway *et al.* [78], but their results are normalized by T_{350}. Wechsler *et al.* [79] recommended an exponential function for $T > T_{350}$. For a detailed discussion of the numerical procedures and results provided by this multilayer force-restore method see Kramm *et al.* [29]. As mentioned before, **Figures 1(b)-(d)** and **Figure 2** are based on the results provided by this multilayer force-restore method.

3. ASTROMETRIC ASPECTS

The local energy budget equation for a thin slab of the regolith adjacent to the surface of either the Moon or the Earth in the absence of its atmosphere given by Equations (2.1), (2.3), and (2.5) as well as the local radiation budget expressed by Equation (1.12) requires the solar input. For computing the TSI, we need Equation (1.7), the solar constant, and the local zenith distance of the Sun's center.

In the case of the Earth, $\cos\Theta_0$ can be determined using the rules of spherical trigonometry (e.g., [8, 9, 36, 80-85])

$$\begin{aligned} \cos\Theta_0 &= \sin\phi\sin\delta_S + \cos\phi\cos\delta_S\cos h \\ &= \cos\theta\sin\delta_S + \sin\theta\cos\delta_S\cos h \end{aligned} \tag{3.1}$$

Here, δ_S is the declination of the Sun, ϕ is latitude, and h is the hour angle with respect to the local meridian. We use a spherical coordinate frame with its origin in the center of a planet or a natural sa-

tellite, the zenith angle, θ, is counted with respect to the body's rotation axis, which shows in the direction of the Northern Celestial Hemisphere. The declination of the Sun can be determined using

$$\sin\delta_S = \sin\varepsilon\sin\lambda = \sin\varepsilon\sin(\upsilon+\varpi) \tag{3.2}$$

where ε is the obliquity of the ecliptic, and $\lambda = \upsilon + \varpi$ is the true longitude of the Earth counted counterclockwise from the vernal equinox (e.g., [8, 9, 84, 86, 87]), υ is the true anomaly, *i.e.*, the positional angle of the Earth on its orbit counted counterclockwise from the Perihelion, and ϖ is the longitude of the Perihelion counted counterclockwise from the moving vernal equinox of the Northern Hemisphere. The declination δ_S ranges from $\delta_S = 23^\circ 26' 21''\text{S}$ (Tropic of Capricorn; $\lambda = 3\pi/2$) to $\delta_S = 23^\circ 26' 21''\text{N}$ (Tropic of Cancer; $\lambda = \pi/2$), and h ranges from $-H$ to H, where H represents the half-day, *i.e.*, from sunrise to solar noon or solar noon to sunset. The half-day must fulfill the condition $H < \pi$, where π corresponds to 12 hours. This condition is not fulfilled for those points within the polar domes delimited by the polar circles for which the Sun does not set within 24 hours, because then $\cos\Theta_0 = 0$ does not hold [81, 82]. Therefore, the condition $H = \pi$ is that of the polar circle, *i.e.*, $\phi = -66^\circ 33' 39''$ (Antarctic circle) and $\phi = 66^\circ 33' 39''$ (Arctic circle). Furthermore, the obliquity is given by $\varepsilon = \bar{\varepsilon} + \Delta\varepsilon$, where the mean obliquity of date,

$$\bar{\varepsilon} = 84381''.448 - 46''.815T - 0''.00059T^2 + 0''.001813T^3 \tag{3.3}$$

is adopted from Folkner *et al.* [88] and Park *et al.* [89]. The nutation in the obliquity is given, for instance, by $\Delta\varepsilon = 9''.205348\cos\Omega$ [88], where the ascending node of Moon's orbit on the ecliptic reads [88, 89]

$$\Omega = 125^\circ 02' 40''.280 - 1934^\circ 08' 10''.549T + 7''.455T^2 + 0''.008T^3 \tag{3.4}$$

Here, T is the TDB time in centuries with respect to J2000.0, where the Julian century corresponds to 36525 *d*.

For the Moon, δ_S has to be replaced by the selenographic latitude, b_S, of the Sun. In accord with Taylor *et al.* [90], Kramm *et al.* [29] computed the selenographic longitude, l_S, and the selenographic latitude, b_S, of the Sun using

$$\tan(l_S + L_M - \Omega) = \frac{\cos I\cos\beta_H\sin(\lambda_H - \Omega - \Delta\psi) - \sin I\sin\beta_H}{\cos\beta_H\cos(\lambda_H - \Omega - \Delta\psi)} \tag{3.5}$$

and

$$\sin b_S = -\sin I\cos\beta_H\sin(\lambda_H - \Omega - \Delta\psi) - \cos I\sin\beta_H \tag{3.6}$$

where the selenographic colongitude is $90^\circ - l_S$. Here, $I = 5553''.6 \cong 1.54267^\circ$ is the inclination of the ecliptic to the mean lunar equator adopted from Newhall and Williams [91], L_M is the mean longitude of the Moon adopted from Simon *et al.* [92], and $\Delta\psi$ is the nutation in longitude given, for instance, by $\Delta\psi = -17''.206262\sin\Omega$ [88]. Kramm *et al.* [29], however, used the data provided by the planetary and lunar ephemeris DE430 of the Jet propulsion Laboratory (JPL), California Institute of Technology. Since 2020, JPL's planetary and lunar ephemeris DE440 is available [89]. Therefore, we confirmed the astrometric results of Kramm *et al.* from 2017 using DE440. In some cases, we compared our astrometric results with those from the JPL Horizons on-line solar system (https://ssd.jpl.nasa.gov/horizons/) that are based on DE441 because these results are provided by independent calculations.

The heliocentric ecliptic latitude and longitude of the Moon, β_H and λ_H, are given by

$$\sin\beta_H = \frac{Z_{SM}}{d_{SM}} \tag{3.7}$$

and

$$\tan\lambda_H = \frac{Y_{SM}}{X_{SM}} \tag{3.8}$$

Here, $d_{SM} = |\boldsymbol{d}_{SM}|$ is the length of the heliocentric vector to the Moon, $\boldsymbol{d}_{SM} = (X_{SM}, Y_{SM}, Z_{SM})$ with the coordinates X_{SM}, Y_{SM}, and Z_{SM}. Kramm *et al.* [29] also used JPL's DE430 to compute the heliocentric distances of the Moon, r_M, and the Earth, r_E, the declination, δ_S, and the selenographic latitude, b_S, of the Sun, respectively.

Results for these quantities obtained for about twenty synodic months (about 591 days) starting May 24, 2009, 00:00 UT1 (TDB = 2454975.5), denoted hereafter as Period I, are illustrated in **Figure 4(a)** and **Figure 5**, respectively. Based on Equation (1.7) and the values of r_M, r_E, and S, the corresponding TSI reaching either the Moon or the Earth are predicted as well (**Figure 4(b)**). The results illustrated in **Figure 4(a)** lead to a mean heliocentric distance for the Moon of 1.0012479 AU and for the Earth of 1.00166376 AU, where 1 AU = 149597870.700 km. Since the multilayer-force-restore method has to be spun up to equilibrium prior to analysis of the results [93], only the results provided by it for the last twelve synodic months starting January 15, 2010, 07:11 UT1 (TDB = 2455211.8, New Moon), hereafter denoted as Period II, were analyzed by Kramm *et al.* [29].

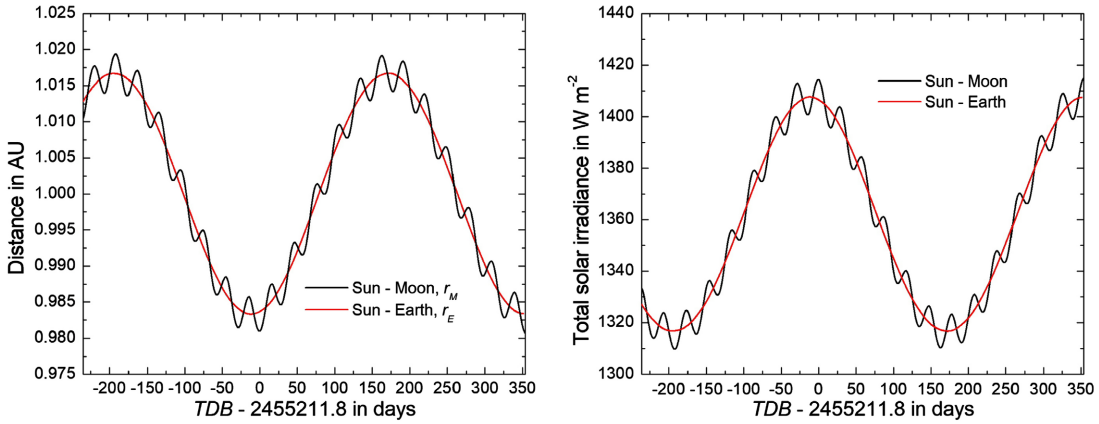

Figure 4. Variation of (a) the heliocentric distances of the Moon, r_M, and the Earth, r_E, during the Period I, derived from the data provided by JPL's ephemeris DE430, and (b) the TSI reaching the sub-solar point either of the Earth or Moon as obtained with Equation (1.7) for $S = 1361\ \mathrm{W \cdot m^{-2}}$.

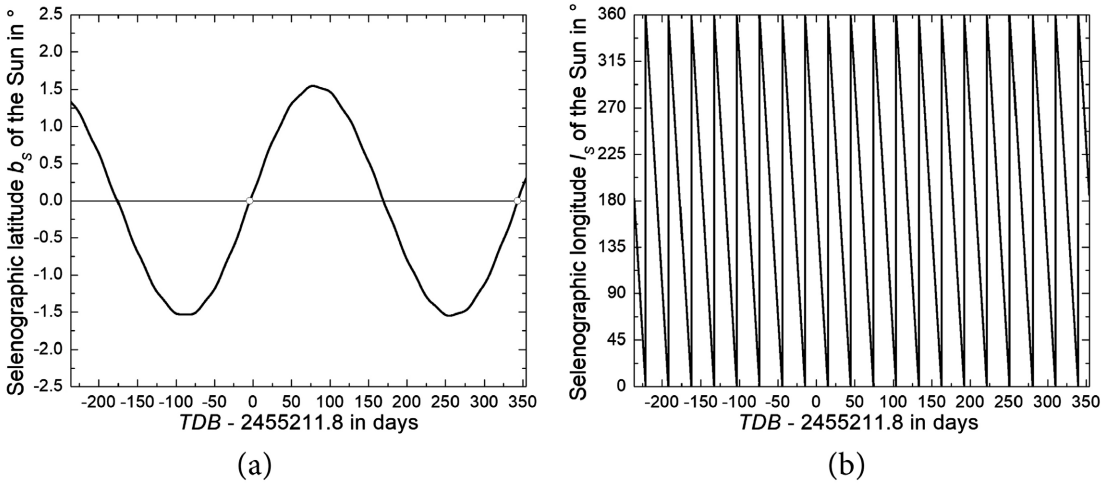

Figure 5. Variation of (a) the selenographic latitude, b_S, and (b) the selenographic longitude, l_S of the Sun during the Period I. The results are based on the data provided by JPL's ephemeris DE430.

The synodic month (also referred to as a lunation) is defined as the interval between two consecutive New Moons. It is nearly 2.21 days longer than the lunar orbital period with respect to the fixed stars called the sidereal month (see **Table 1**). While the Moon revolves around Earth, both objects also progress in orbit around the Sun. After completing one revolution with respect to the fixed stars, the Moon must continue a little farther along its orbit to catch up to the same position it started from relative to the Sun and Earth [94].

At the time of the New Moon, solar radiation reaches a local maximum. Thus, the calculation of the TSI requires an accurate determination of the New Moon. It occurs when the geocentric ecliptic longitudes of the Sun (λ_S) and the Moon (λ_M) are the same (e.g., [94-96]), customarily expressed by $f(t)=0$, where $f(t)=\lambda_M-\lambda_S$ for New Moon $f(t)=\lambda_M-\lambda_S-90^\circ$ for the first quarter, $f(t)=\lambda_M-\lambda_S-180^\circ$ for the Full Moon, and $f(t)=\lambda_M-\lambda_S-270^\circ$ for the last quarter. Because the times are determined from geocentric coordinates, they are independent of location on the Earth [96]. The variation of λ_M and λ_S as well as the New Moons are illustrated in **Figure 6**. This figure also shows the variation of the ecliptic z coordinate z_{ecl}.

Table 1. Mean values of the different orbital periods.

Orbital period	Duration					Source
	[day]	[hour]	[min]	[sec]	[day]	
Sidereal month (fixed star to fixed star)	27	7	43	12	27.32167	[94-100]
Tropical month (equinox to equinox)	27	7	43	5	27.32159	[94, 96, 98, 100]
Synodic month (New Moon to New Moon)	29	12	44	3	29.53059	[94-100]
Draconic month (node to node)	27	5	5	36	27.21222	[94-96, 98-100]
Anomalistic month (perigee to perigee)	27	13	18	33	27.55455	[94-96, 98-100]

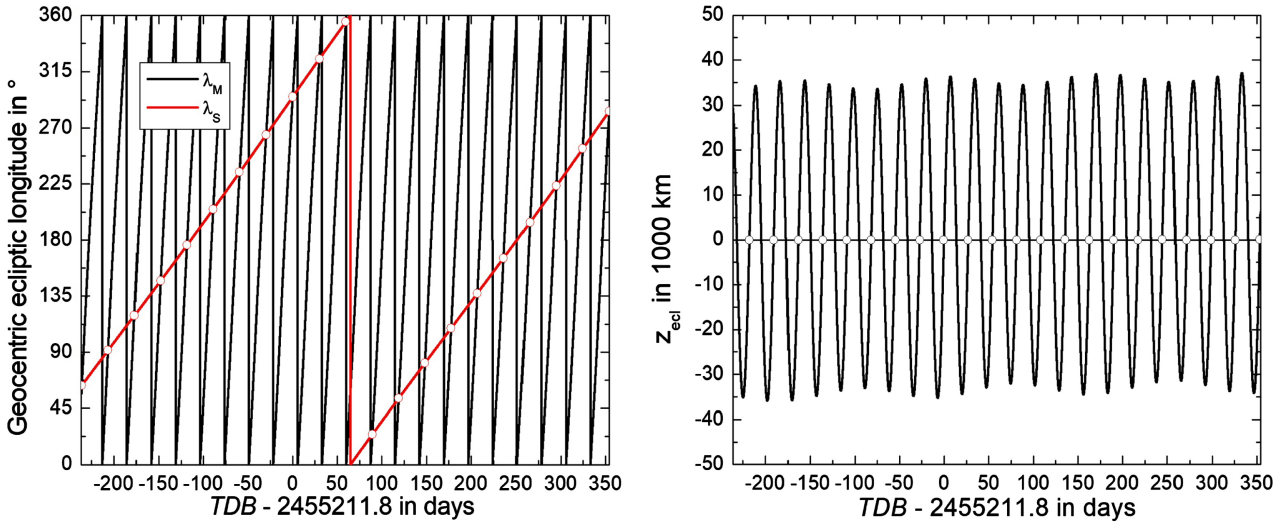

(a) (b)

Figure 6. Variation of (a) the geocentric ecliptic longitudes of the Moon, λ_M, and the Sun, λ_S, and (b) the ecliptic z coordinate, z_{ecl}, for the Period I, derived from the data provided by JPL's ephemeris DE430. The red open circles in (a) represent the New Moons, and the black open circles in (b) the passages of the Moon through the ascending node, respectively.

According to astrometric calculations of Kramm *et al.* [29], the first New Moon of Period I took place on May 24, 2009, 12:09 UT1 and the last one on January 4, 2011, 8:59 UT1. As listed in **Table 1**, the mean synodic month is about 29.53059 days. However, as illustrated in **Figure 7(a)**, the true lunation deviates from the mean one by up to seven hours during the Period I. For this period, the results differ from those derived by Roncoli [101] using JPL's ephemeris DE403/LE403 by less 420 s, *i.e.*, within the range of the maximum time step of about 600 s used by Kramm *et al.* during the integration of Equation (2.3).

Obviously, the reliable determination of the New Moon requires accurate astrometric calculations of the geocentric ecliptic longitudes of the Sun (λ_S) and the Moon (λ_M). It can be achieved the best within the framework of the calculation of well-known geocentric quantities of the Moon.

The geocentric distance, the astrometric right ascension, and the declination of the Moon for the Period I are illustrated in **Figure 8**. As shown in **Figure 8(a)**, the perigee distance varies significantly more with time than the apogee distance. According to our astrometric calculations, Moon's perigee distance ranges from 356,593 km to 369,733 km while the apogee distance only ranges from 404,167 km to 406,541 km during the Period I. The corresponding mean geocentric distance of the Moon amounts to 384,792 km.

The actual geocentric distance of the Moon is given by

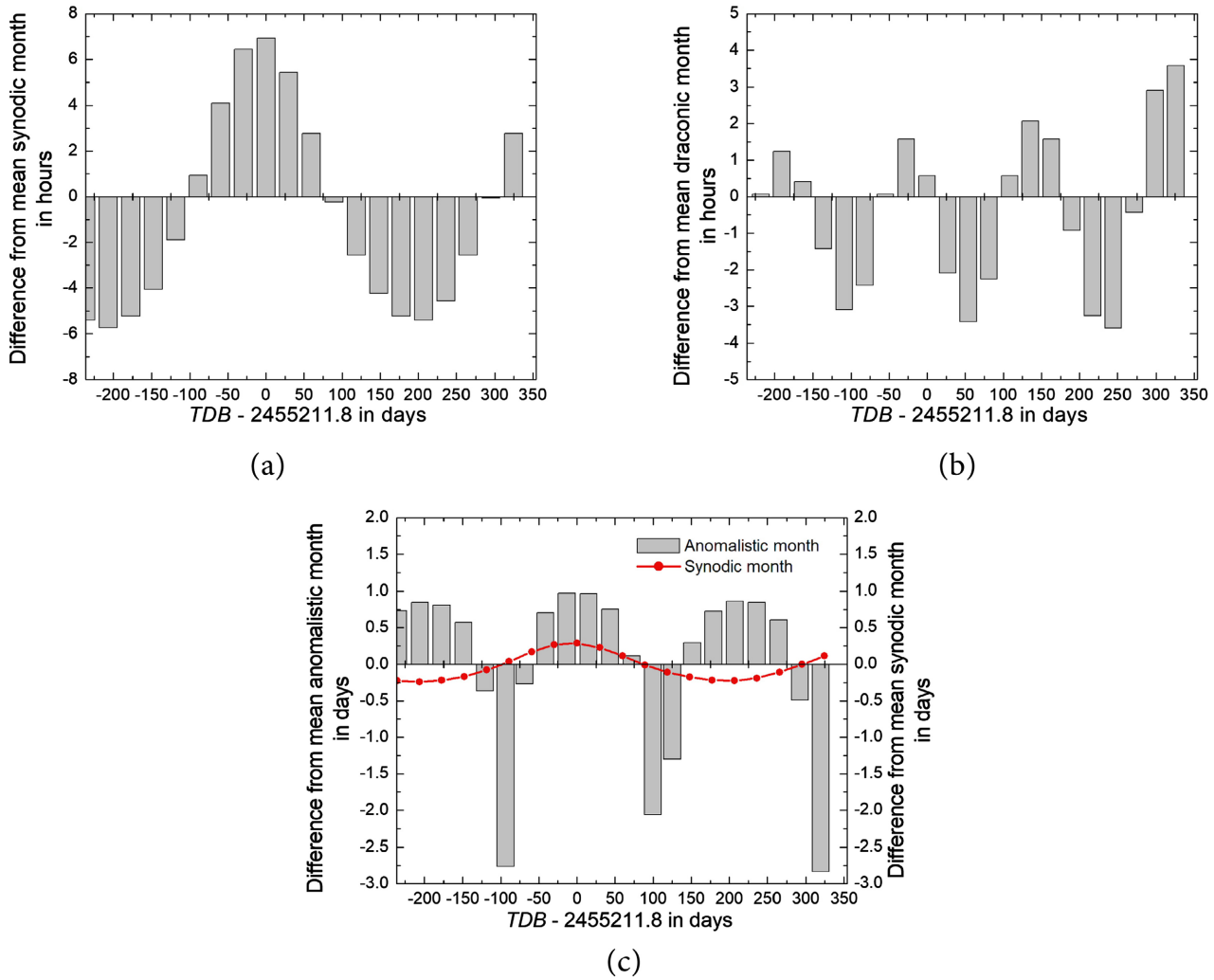

Figure 7. Difference from (a) the mean synodic month, (b) the mean draconic month, and (c) the mean anomalistic month and the mean synodic month for the Period I, derived from the data provided by JPL's ephemeris DE430.

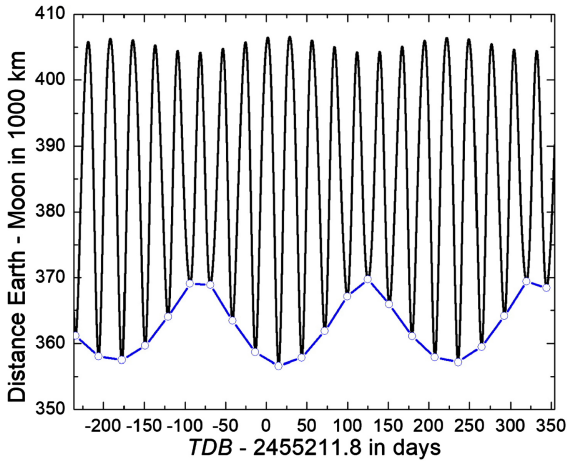

(a)

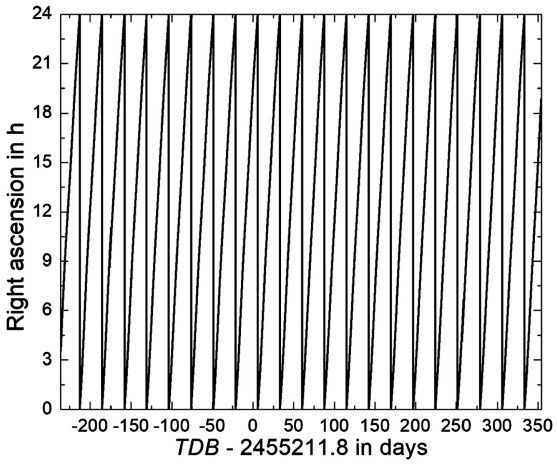

(b)

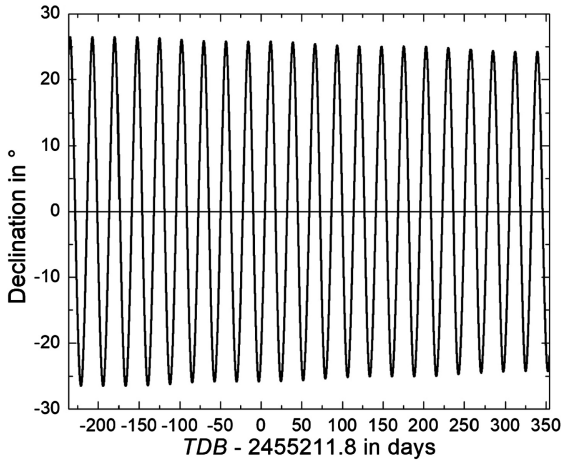

(c)

Figure 8. Variation of (a) Moon's geocentric distance, (b) the astrometric right ascension, and (c) the declination of the Moon's center during the Period I, derived from the data provided by JPL's ephemeris DE430. The blue open circles in (a) mark the perigee.

$$r = +\sqrt{x_{eq}^2 + y_{eq}^2 + z_{eq}^2} \tag{3.9}$$

Here, x_{eq}, y_{eq}, and z_{eq} are the equatorial coordinates, where x_{eq} points to the first point of Aries that corresponds to the vernal equinox of the Northern Hemisphere. These equatorial coordinates are provided by JPL's ephemeris DE430.

Perigee and apogee can simply be determined using the first and second derivative tests. In accord with Equation (3.9), the first derivative of the actual geocentric distance with respect to time is given by

$$\frac{\mathrm{d}r}{\mathrm{d}t} = \frac{1}{r}\left(x_{eq}\frac{\mathrm{d}x_{eq}}{\mathrm{d}t} + y_{eq}\frac{\mathrm{d}y_{eq}}{\mathrm{d}t} + z_{eq}\frac{\mathrm{d}z_{eq}}{\mathrm{d}t} \right) \tag{3.10}$$

The ephemeris DE430 provides both the components of the position vector and the components of the velocity vector for computing this derivative. The optimum is given when the expression in parentheses is equal to zero (*i.e.*, $\mathrm{d}r/\mathrm{d}t \cong 0$). The sign of the second derivative for the time of the optimum marks either the perigee ($\mathrm{d}^2r/\mathrm{d}t^2 > 0$) or the apogee ($\mathrm{d}^2r/\mathrm{d}t^2 < 0$). Because $\mathrm{d}^2x_{eq}/\mathrm{d}t^2$, $\mathrm{d}^2y_{eq}/\mathrm{d}t^2$, and

$d^2 z_{eq}/dt^2$ are not delivered by the ephemeris, we determine the second derivative numerically from the dr/dt curve. The results for about twelve anomalistic months of 2010 are illustrated in **Figure 9**.

In addition to the sidereal and synodic months, three other orbital periods or months are distinguished (e.g., [94-96, 99]): 1) The orbital period with respect to the equinox called the tropical month, 2) the draconic (or nodical) month defined as the interval between two successive passages of the Moon through the ascending node (see **Figure 6(b)**), and 3) the anomalistic month related to the interval required by the Moon to move in its path around the Earth from perigee to perigee (see **Figure 8(a)**).

It is well-known that the lengths of these different months vary with time (e.g., [94, 100]). For convenience, their mean values are listed in **Table 1**. The deviations of these different months from their mean values during the Period I are illustrated in **Figure 7**. While the synodic and draconic months deviate from their mean values only by hours, the anomalistic month departs from its mean even by days. The largest negative deviations occur around the points of inflection in the curve representing the departure of the synodic month from its mean (see **Figure 7(c)**).

As pointed out by Paige *et al.* [57], the Moon experiences seasonal insolation variations due to the combined effects of the 5.14˚ obliquity of the Moon's orbital plane relative to the ecliptic, and the 6.68˚ obliquity of the Moon's spin axis relative to the Moon's orbital plane. The net effect is that the latitude of the subsolar point undergoes a seasonal variation with an amplitude of about 1.54˚ and a period of about 346 days, which is less than a full Earth year due to the precession of the Moon's orbital plane. According to **Figure 5(a)**, the time interval between the two passages of the Sun through the ascending node (characterized by the open circles) of the lunar equator plane corresponds to 347.29 days, *i.e.*, it is slightly longer than the mean draconic year of 346.62 days [57, 96, 99] that is based on the 223 synodic months of the Saros period of about $18^a11^d8^h$ and 19 eclipse years [94, 99, 100]. Based on our calculations, these ascending nodes are related to January 11, 2010, 2:24:00 UT1 (TDB = 2455207.60) and December 24, 2010, 9:21:36 UT1 (TDB = 2455554.89). The draconic year is connected with the occurrence of eclipses [99, 102].

4. MODEL RESULTS

The variations of the solar insolation and the absorbed solar radiation, and the soil heat flux at the depths of 2 cm for numerous parallels of latitude for Moon's northern and southern hemispheres predicted

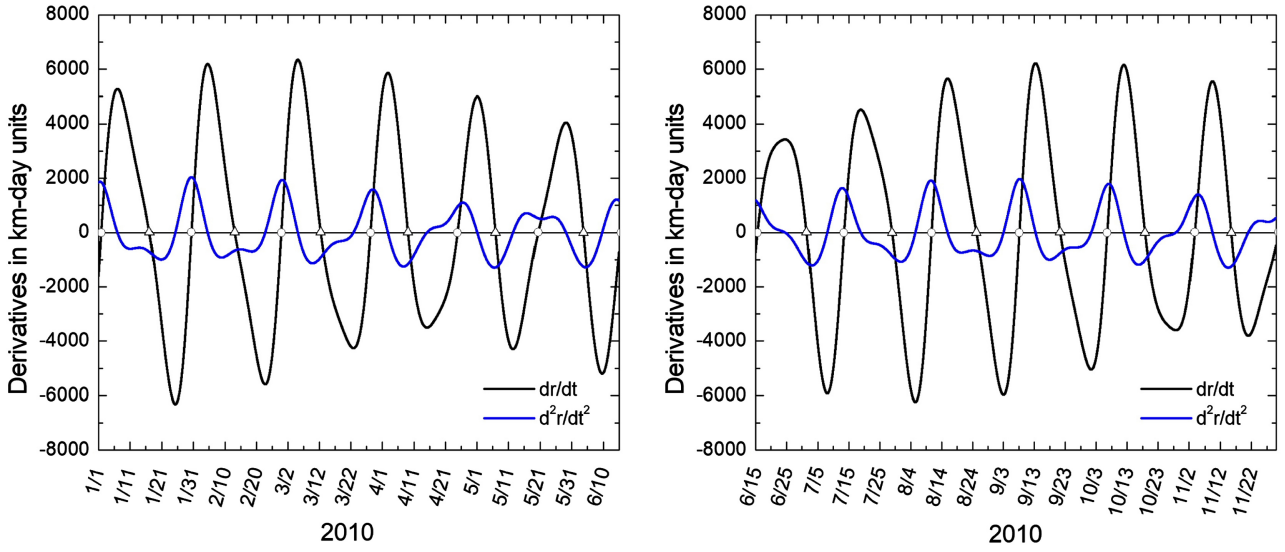

Figure 9. First and second derivative tests for determining the perigee ($dr/dt \cong 0$ and $d^2r/dt^2 > 0$, open circles) and the apogee ($dr/dt \cong 0$ and $d^2r/dt^2 < 0$, open triangles) for about twelve anomalistic months of 2010. The results are based on the data provided by JPL's ephemeris DE430.

for the Period II are illustrated in Figure 10. The distributions of the daily mean values of the solar insolation at Moon's surface and the absorbed solar radiation predicted for this period are illustrated in Figure 1(c) and Figure 1(d), respectively. The variations of the respective slab temperatures are illustrated in Figure 11.

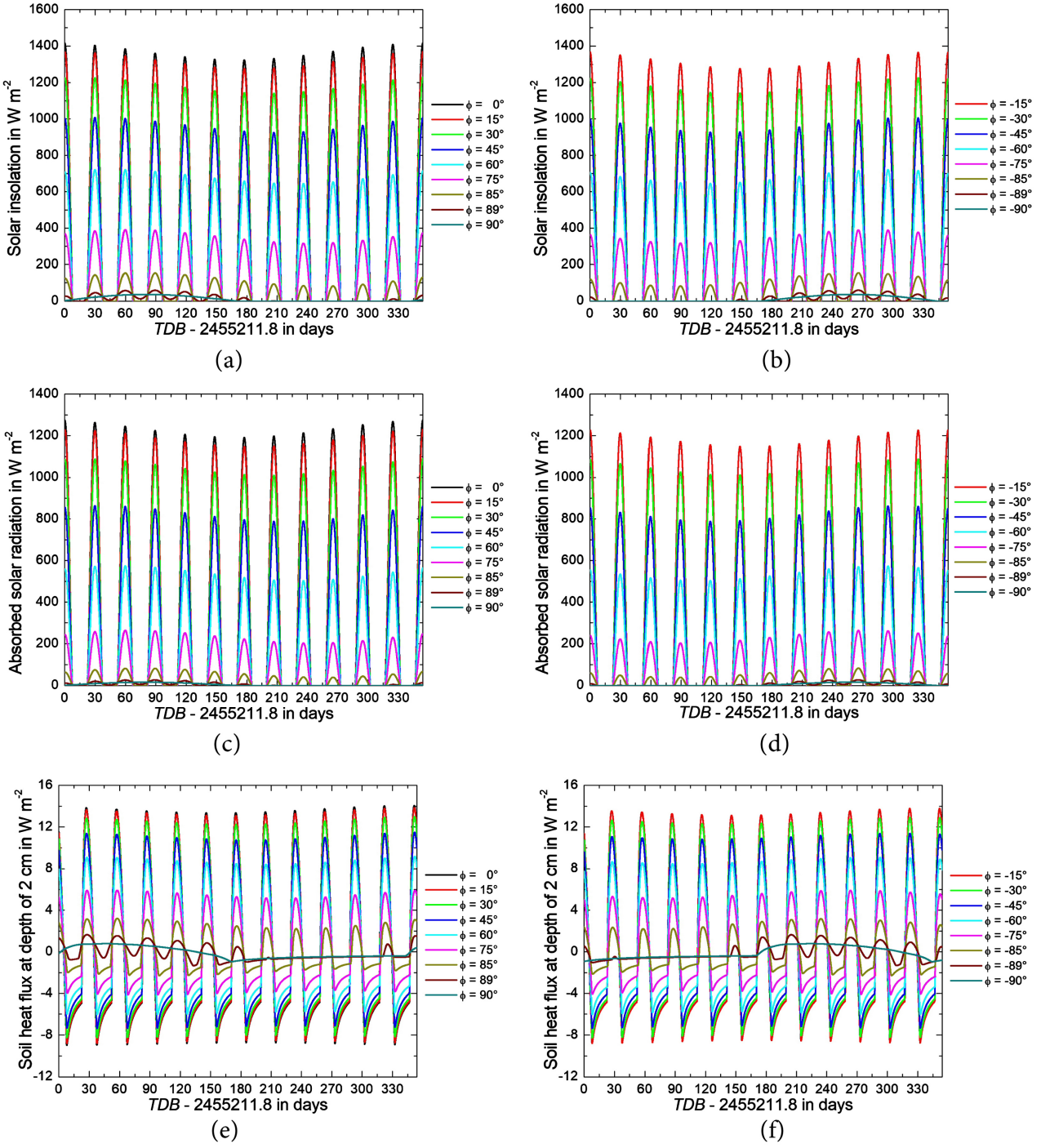

Figure 10. Variations of the solar insolation and the absorbed solar radiation at the surface, and the soil heat flux at the depths of 2 cm for various parallels of latitude for Moon's northern hemisphere ((a), (c), (e)) and southern hemisphere ((b), (d), (f)) predicted for the Period II.

Since the rotation axis of the Moon is tilted at an angle of about 1.54˚ with respect to the normal of the ecliptic plane, the lunar polar circles are located at latitudes of ±88.46˚ and insolation conditions at these lunar latitudes depend on both local time and season [57]. **Figure 10** and **Figure 11** already illustrate this dependence, but **Figure 12** and **Figure 13** exhibit this dependence in a more convenient manner. They illustrate the variations of the solar insolation and the local surface temperature T_s at latitudes of 89˚N, 90˚N, 89˚S and 90˚S for the respective white nights of the polar regions, where T_s is based on a local radiative equilibrium expressed by Equation (1.12). For comparison, the local slab temperature T_{slab} provided by the multilayer-force restore method is illustrated as well. Obviously, the thermal inertia of the system, expressed by the thermal inertial coefficient R_t in Equation (2.3) and the heat flow H_{sl} in the regolith, are responsible for the differences between T_s and T_{slab}. Outside these polar white nights, T_s drops to 0 K during nighttime. Therefore, Equation (1.12) is an unsuitable approximation of Equations (2.3) and (2.5). for most regions of the Moon, as already demonstrated by Wesselink [62].

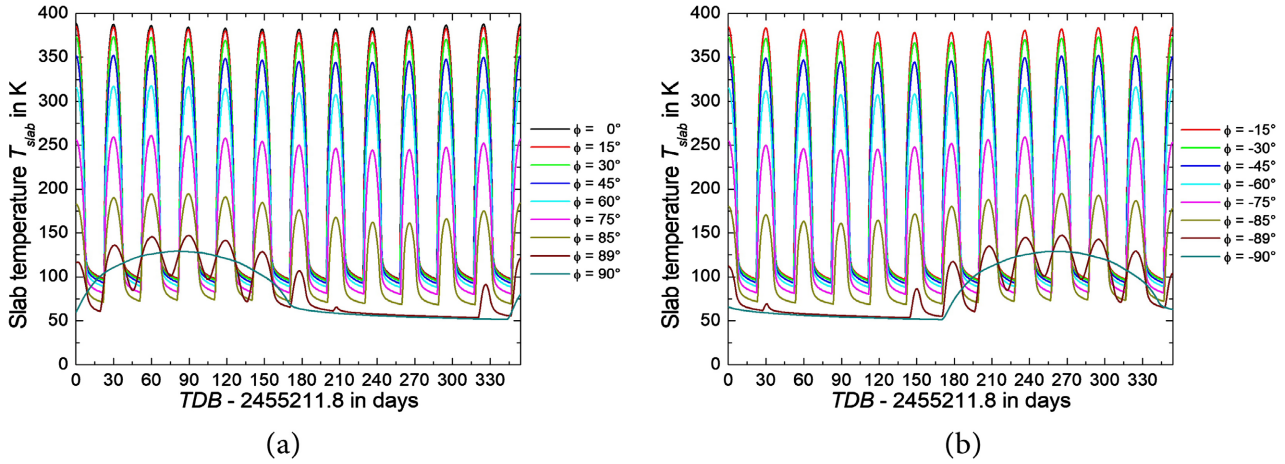

Figure 11. Variations of the slab temperature for numerous parallels of latitude for Moon's northern hemisphere (a) and southern hemisphere (b) during Period II (adopted from Kramm *et al.* [29]).

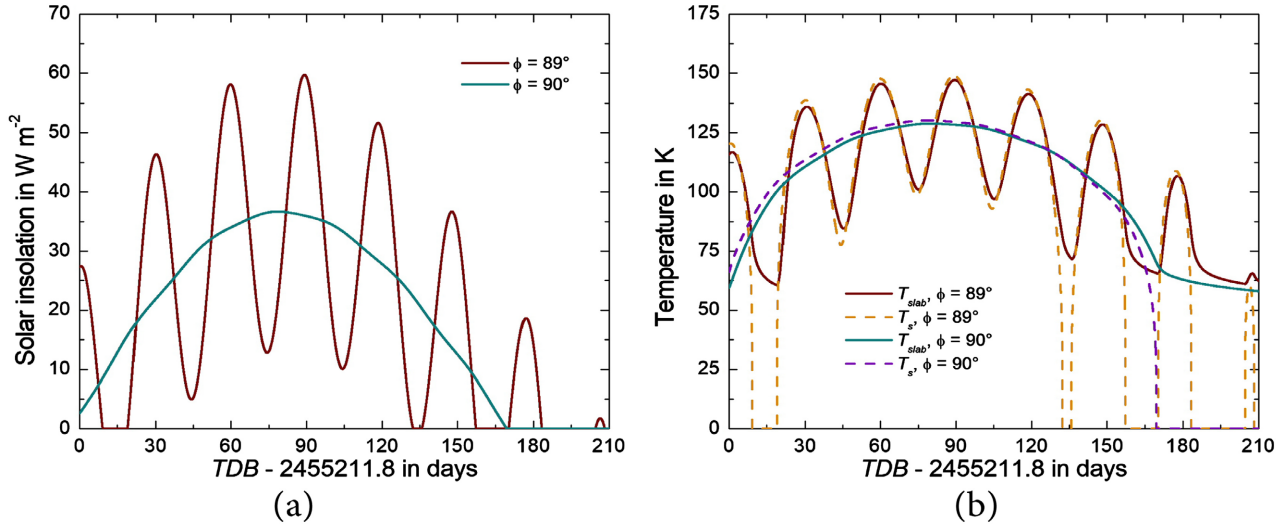

Figure 12. Variation of (a) the solar insolation and (b) the surface temperature T_s given by Equation (1.12) and the slab temperature T_{slab} according to Equation (2.3) for a white night of the polar region of the northern hemisphere.

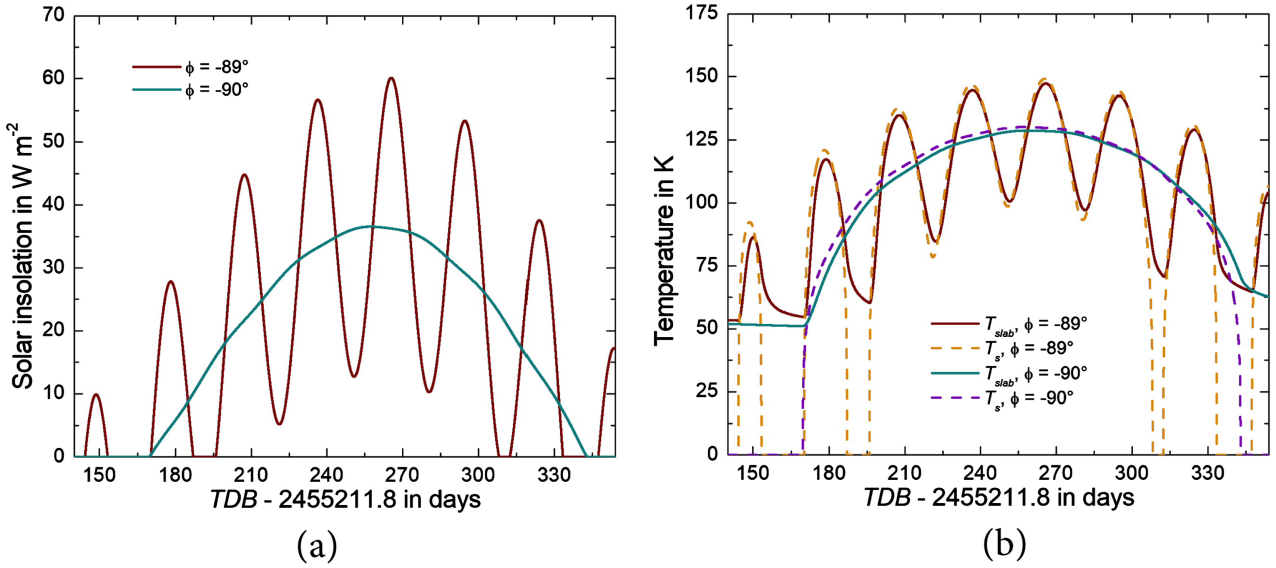

Figure 13. As in Figure 12, but for a white night of the polar region of the southern hemisphere.

According to Espenak and Meeus [94, 100], an annular solar eclipse occurred on January 15, 2010, and a total lunar eclipse occurred on December 21, 2010 (Saros 125). The latter occurred during the twelfth lunation of the Period II. Furthermore, a partial lunar eclipse occurred on June 26, 2010 (Saros 120). To estimate the effect of these two lunar eclipses on the global mean of the surface temperature, we considered the surface temperature measurements performed at the landing site of the Apollo 15 mission, Hadley Rille/Apennine Mountains (26˚5'N, 3˚40'E,) from July 31, 1971 to December 31, 1974 during the Heat Flow Experiment using the Apollo Lunar Surface Experiment Package (ALSEP) [72]. From this dataset, we considered the period from January 8, 1974 (Full Moon) to December 29, 1974 (Full Moon) that is comparable with twelve synodic months. Figure 14 shows the time series TC2 of the probe 2 at the Hadley Rille site, the partial lunar eclipse from June 4, 1974 (Saros 120), and the total lunar eclipse from November 29, 1974 (Saros 125). A comparable drop in the surface temperature of about 220 K during a total lunar eclipse was already observed and modeled by Fontain *et al.* (1976). From this time series at the Hadley Rille site, we computed the zonal average of the surface temperature by including these two lunar eclipses. We obtained a zonal average of 201.9 K. Then, we repeated our calculation by considering the same dataset in which, however, the effects of these lunar eclipses were arbitrarily removed by using an interpolation procedure for bridging the surface-temperature decreases. Ignoring these lunar eclipses leads to a zonal average of 202.0 K, *i.e.*, without the two lunar eclipses the zonal average would be 0.1 K higher.

5. THE DIVINER LUNAR RADIOMETER EXPERIMENT

The Diviner Lunar Radiometer Experiment (DLRE) is one of seven instruments aboard NASA's Lunar Reconnaissance Orbiter (LRO) [59-61]. The LRO was launched on June 18, 2009 and entered a lunar orbit five days later. Beside the exploration mission of the LRO not considered here, the DLRE was the first experiment to systematically map the global thermal state of the Moon and its diurnal and seasonal variability [57]. Paige *et al.* [57] described the instrument, its specifications, the spectral channel passbands, and the archived data products in detail. The data are based on a nine-channel radiometer that maps solar reflectance using channels 1 and 2 of high and reduced sensitivity (0.35 - 2.8 μm passband), and infrared emission using four thermal channels, where channel 6 (13 - 23 μm passband) is most sensitive for $T_s > 178\,\mathrm{K}$, channel 7 (25 - 41 μm passband) is most sensitive for $69\,\mathrm{K} \le T_s \le 178\,\mathrm{K}$, channel 8 (50 - 100 μm passband) is most sensitive for $43\,\mathrm{K} \le T_s \le 69\,\mathrm{K}$, and channel 9 (100 - 400 μm passband) is most sensitive for $T_s < 43\,\mathrm{K}$. Figure 15 shows the nine spectral passbands of the DLRE. The respective blackbody

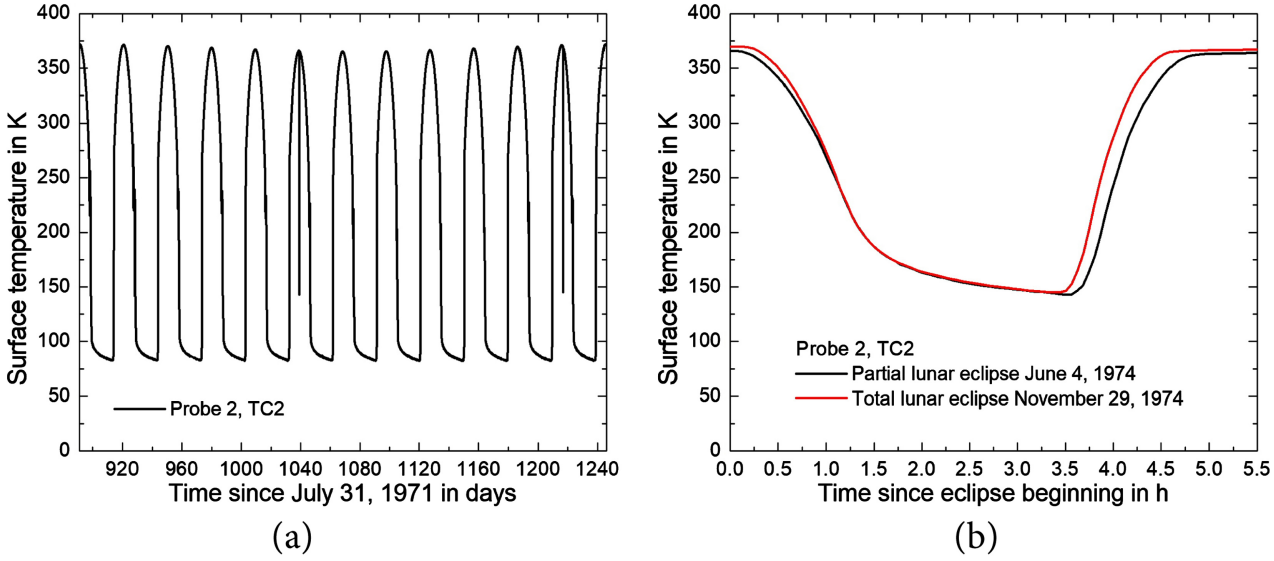

Figure 14. (a) Thermocouple temperature TC2 of the probe 2 at the landing site Hadley Rille/Apennine Mountains (26˚5'N, 3˚40'E) of the Apollo 15 for twelve synodic months, (b) partial lunar eclipse from June 4, 1974 (Saros 120), and total lunar eclipse from November 29, 1974 (Saros 125).

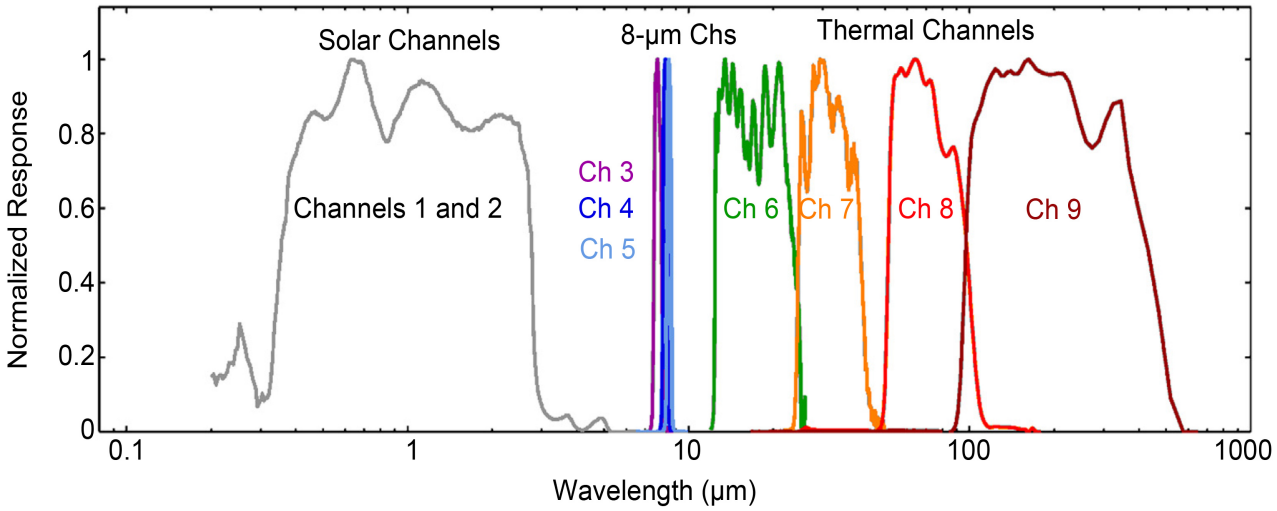

Figure 15. The nine spectral passbands of the Diviner Lunar Radiometer Experiment (DLRE) [39].

curves for both the solar range at 1 AU and for various possible surface temperature of the Moon in the infrared range based on Planck's [103] radiation function are illustrated in **Figure 16**.

The bolometric temperatures of the DLRE is a measure of the spectrally integrated flux of infrared radiation emerging from the surface [104]. These bolometric temperatures are available since April 2018 under http://luna1.diviner.ucla.edu/~jpierre/diviner/level4_raster_data/ (referenced to Williams *et al.* [39]). They comprise 24 datasets for various subsolar longitudes ranging from $\phi_{ss} = 0^{\circ}\mathrm{E}$ to $\phi_{ss} = 345^{\circ}\mathrm{E}$, spaced by $\Delta\phi_{ss} = 15^{\circ}$. Williams *et al.* [39] compiled all nadir observations (defined to be emission angles <10˚ relative to a sphere) from July 5, 2009 to April 1, 2015 (over 25,000 orbits) into bins of 0.5˚ latitude and longitude and 0.25 h of local time. Because these authors discussed the accuracy of the DLRE observations in detail, the reader is referred to their paper and the cited sources, especially [57, 104-107].

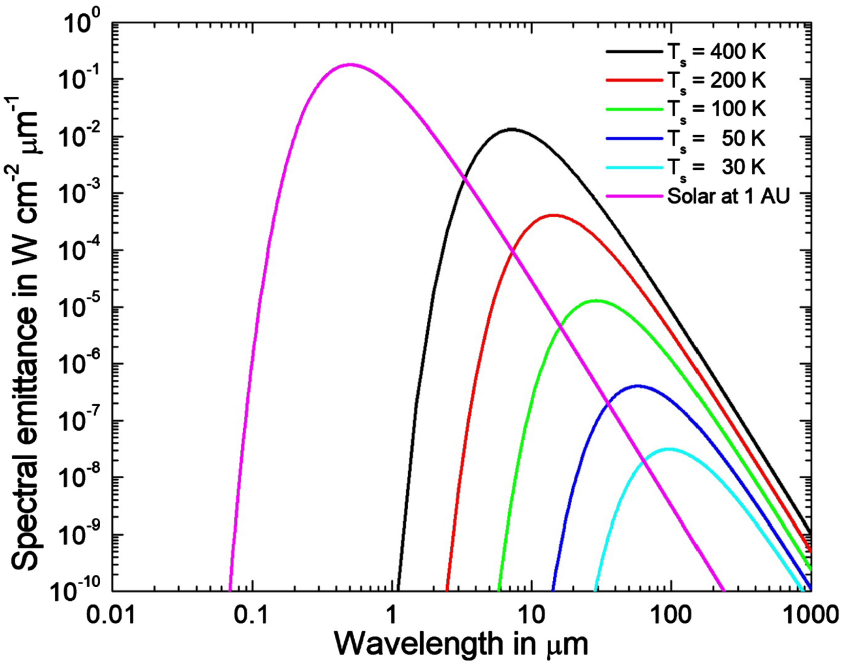

Figure 16. Representative blackbody curves for the solar range at 1 AU and for various possible surface temperature of the Moon in the infrared range that are based on Planck's [103] blackbody radiation function (adopted from Paige *et al.* [57], but with the solar spectral emittance at 1 AU added).

6. MODEL RESULTS VERSUS DLRE OBSERVATIONS

Figure 17 and **Figure 18** illustrate the results of the comparison between T_{slab} of the eleventh lunation shown in **Figure 11** (which is close in length to the mean synodic month, see **Figure 7(a)**) and T_{bol} of the DLRE related to the subsolar longitude $\phi_{ss} = 180^{\circ}\text{E}$ [39] for the equator and various parallels of latitude of the northern hemisphere and the southern hemisphere, respectively. Obviously, the predicted slab temperatures follow the bolometric temperatures acceptably. Between 75˚N and 75˚S, (most important to compute $\langle T_{slab} \rangle$ and $\langle T_{bol} \rangle$, respectively, see **Figure 19**), the zonally averaged differences and the respective standard deviations are: 3.5 K ± 12.0 K for 75˚N 1.4 K ± 8.0 K for 60˚N, 0.9 K ± 6.5 K for 45˚N, 0.7 K ± 6.4 K for 30˚N, 0.4 K ± 6.3 K for 15˚N, 0.3 K ± 5.8 K for 0˚, 0.0 K ± 5.1 K for 15˚S, 0.1 K ± 5.8 K for 30˚S, 0.4 K ± 6.3 K for 45˚S, −0.4 K ± 8.1 K for 60˚S, and 0.2 K ± 10.2 K for 75˚S.

Figure 19(a) shows meridional distributions of the zonal averages of the bolometric temperature, $\overline{T}_{bol}(\theta)$, for various zenith angles θ that are based on Equation (1.3) choosing $\psi(\theta,\varphi) = T_{bol}(\theta,\varphi)$. These meridional distributions represent the range of all 24 DLRE datasets. **Figure 19(b)** shows the corresponding meridional distributions of $\overline{T}_{bol}(\theta)\sin\theta$, as required by Equation (1.2) for global averaging. Obviously, the higher nighttime temperatures and standard deviations for the polar spherical caps at latitudes beyond ±80˚ (*i.e.*, low and high values of θ) resulting from the occurrence of low-angle illumination of surfaces, especially during polar summers, as already reported by Williams *et al.* [39], are of minor importance in global averaging. **Figure 19** also shows the slab-temperature results of Kramm *et al.* [29] provided by their multilayer force-restore method. These results agree the best with the distribution of the bolometric temperature related to $\phi_{ss} = 180^{\circ}\text{E}$. In this case, $\langle T_{slab} \rangle = 197.9\,\text{K}$ and $\langle T_{bol} \rangle = 200.0\,\text{K}$.

The zonal averages derived from the 24 DLRE datasets and the respective standard deviation for various parallels of latitude are listed in **Table 2**. Also listed are the zonal averages obtained from model simulations using the multilayer-force-restore method [29], and the in-situ measurement of the Apollo 15 and 17 missions using the probe 2 of the Heat Flow Experiment (HFE) of the Apollo Lunar Surface Experiment Package (ALSEP) [72, 73], where the entire periods were considered. Thus, these results slightly

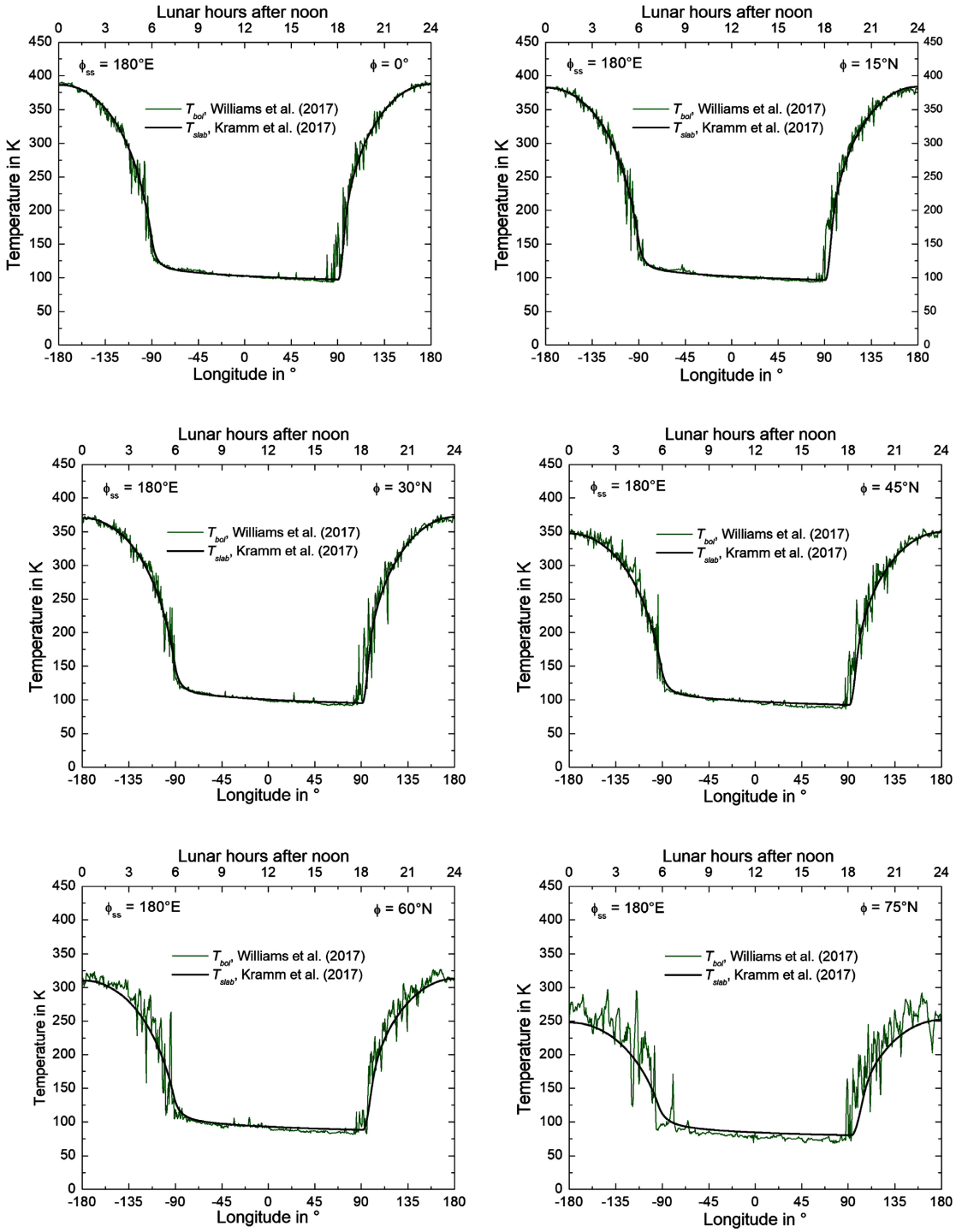

Figure 17. Comparison between the slab temperature, T_{slab}, of the eleventh lunation shown in Figure 11 (adopted from Kramm *et al.* [29]) and the bolometric temperature, T_{bol}, of the Diviner Lunar Radiometer Experiment related to the subsolar longitude $\phi_{ss} = 180°\text{E}$ (with reference to Williams *et al.* [39]) for the Equator and various parallels of latitude of the northern hemisphere. Note that the eleventh lunation is close in length to the mean synodic month (see Figure 7(a)). Furthermore, the T_{bol} curves are averages for the respective parallels of latitude.

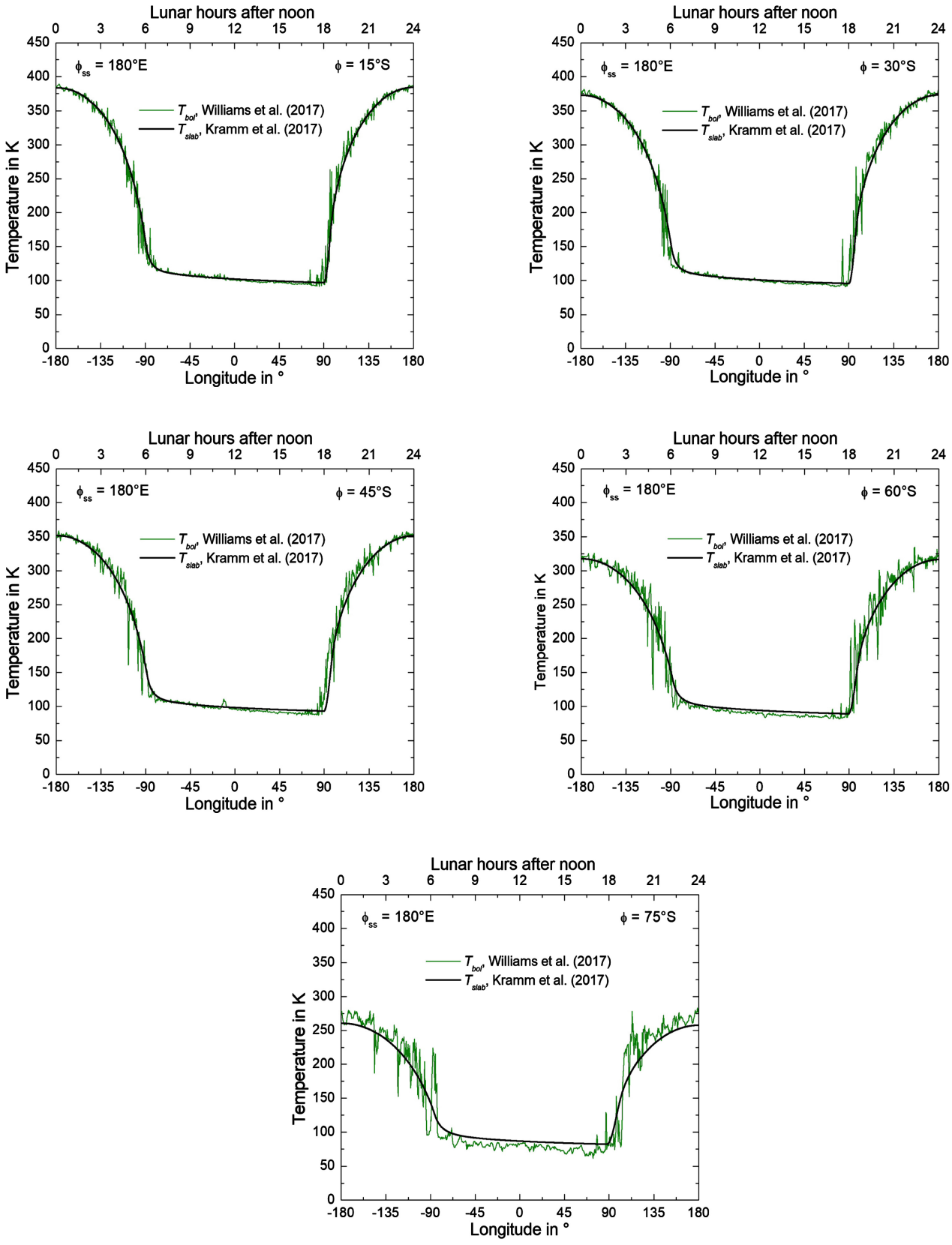

Figure 18. As in Figure 17, but only for the southern hemisphere.

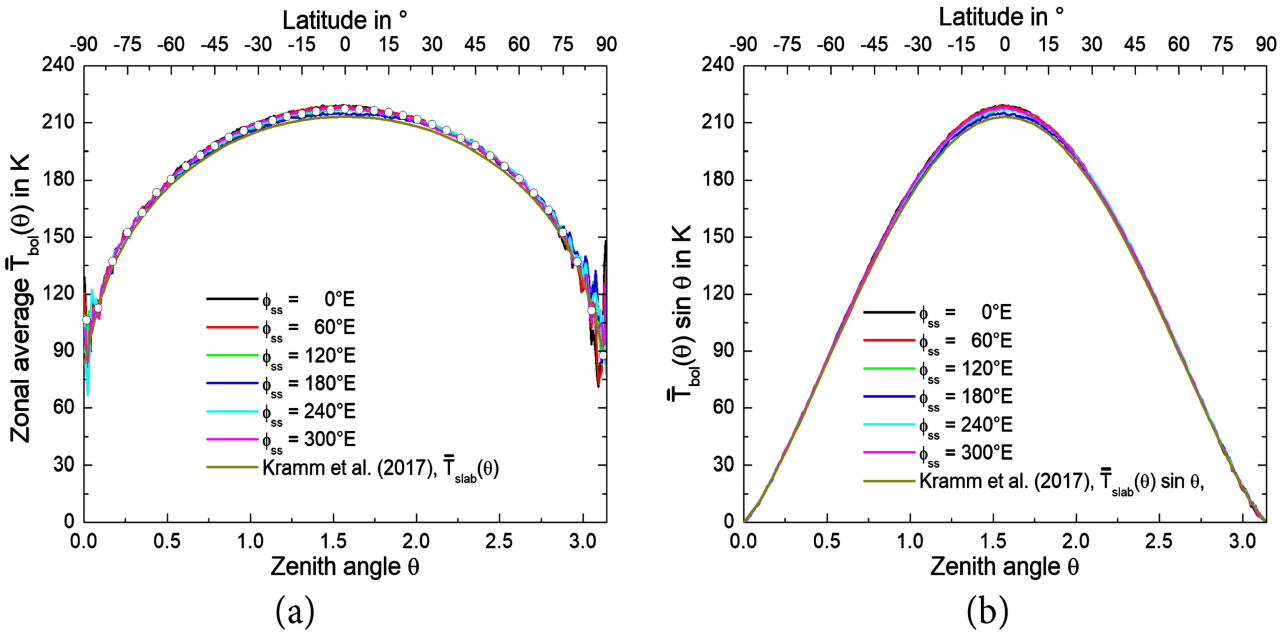

Figure 19. **(a) Typical meridional distributions of the zonal averages (see Equation (1.3)) of the bolometric temperature, $\bar{T}_{bol}(\theta)$, for various values of the zenith angle θ and the subsolar longitude ϕ_{ss}, and (b) the corresponding meridional distributions of $\bar{T}_{bol}(\theta)\sin\theta$ as required by Equation (1.2) for global averaging. The black open circles in (a) represent the zonal averages listed in Table 2 that were derived from the 24 datasets of the Diviner Lunar Radiometer Experiment [39].**

differ from those published by Keihm *et al.* [72] and Keihm and Langseth [73].

The global averages of the bolometric temperature, $\langle T_{bol}\rangle$, for all 24 datasets related to the subsolar longitude ϕ_{ss} are illustrated in **Figure 20**. The arithmetic mean and the standard deviation of this distribution amount to $\langle T_{bol}\rangle = 201.1\,\mathrm{K} \pm 0.6\,\mathrm{K}$. Since $\langle T_{bol}^4\rangle^{1/4} = 271.0\,\mathrm{K} \pm 0.7\,\mathrm{K}$, averaged over these 24 datasets, we have $\langle T_{bol}\rangle \cong 0.742\langle T_{bol}^4\rangle^{1/4}$. This means that the DLRE observations confirm the result $\langle T_{slab}\rangle \cong 0.743\langle T_{slab}^4\rangle^{1/4}$ theoretically derived by Kramm *et al.* [29]. These observations also confirm the temperature inequality (1.17) of Gerlich and Tscheuschner [53].

The meridional distributions of the zonal averages of the absorbed solar radiation, $\bar{Q}(\theta)$, and the emitted infrared radiation, $\bar{F}_{IR}(\theta)$, both weighted by $\sin\theta$ as required for global averaging, are shown in **Figure 21** for different values of the normal albedo and the integral relative emissivity, $\alpha_0 = 0.08$ and $\varepsilon = 0.95$ derived by Williams *et al.* [39] from the DLRE observations, and $\alpha_0 = 0.10$ and $\varepsilon = 0.98$ suggested by Vasavada *et al.* [58] and used by Kramm *et al.* [29] in their model simulations. It seems that in the case of $\phi_{ss} = 180^\circ\mathrm{E}$, the normal $\alpha_0 = 0.08$ is a little bit too low. In this case, the global average of the absorbed solar radiation computed for the twelve lunations analyzed by Kramm *et al.* is $\langle Q\rangle = 288.7\ \mathrm{W\cdot m^{-2}}$ for $\alpha_0 = 0.08$. Whereas the global average of the emitted infrared radiation is $\langle F_{IR}\rangle = 285.7\ \mathrm{W\cdot m^{-2}}$ for $\varepsilon = 0.95$ leading to a radiative imbalance of $\langle Q\rangle - \langle F_{IR}\rangle = 3.0\ \mathrm{W\cdot m^{-2}}$. The predicted results of Kramm *et al.* provided by the multilayer-force-restore method read $\langle Q\rangle = 279.9\ \mathrm{W\cdot m^{-2}}$ for $\alpha_0 = 0.10$ and $\langle F_{IR}\rangle = 280.0\ \mathrm{W\cdot m^{-2}}$ for $\varepsilon = 0.98$ leading to a radiative imbalance of $-0.1\ \mathrm{W\cdot m^{-2}}$.

Based on the globally averaged emitted infrared radiation of $\langle F_{IR}\rangle = 290.5\ \mathrm{W\cdot m^{-2}} \pm 3.0\ \mathrm{W\cdot m^{-2}}$ derived from these 24 datasets (see **Figure 22**), the effective radiative temperature for the Moon would be

Table 2. Zonal averages for various parallels of latitude obtained from model simulations using the multilayer-force-restore method ($\overline{T}_{slab}$) [29], the Diviner Lunar Radiometer Experiment ($\overline{T}_{bol}$) [39], and the in-situ measurement of the Apollo 15 and 17 missions using the probe 2 data of the Heat Flow Experiment (HFE) of the Apollo Lunar Surface Experiment Package (ALSEP) [72, 73].

Latitude in °	$\overline{T}_{slab}$ in K		$\overline{T}_{bol}$ in K		HFE-probe-2 temperature in K		
	NH	SH	NH	SH	TC1	TC2	TC3
0	213.4	-	217.1 ± 1.3	-	-	-	-
5	213.1	213.2	216.9 ± 1.3	216.7 ± 1.3	-	-	-
10	212.6	212.6	216.3 ± 1.3	215.8 ± 1.0	-	-	-
15	211.5	211.5	215.2 ± 1.3	214.6 ± 0.9	-	-	-
20	210.0	210.0	213.7 ± 1.2	213.2 ± 0.7	-	-	-
20.17 (Apollo 17)	-	-	213.6 ± 1.2*	-	220.3	-	-
25	208.1	208.1	211.6 ± 1.2	211.2 ± 0.5	-	-	-
26.08 (Apollo 15)	207.8	-	210.9 ± 1.3#	-	206.5	202.8	198.6
30	205.7	205.6	209.0 ± 1.1	208.5 ± 0.5	-	-	-
35	202.7	202.7	205.7 ± 1.5	205.5 ± 0.4	-	-	-
40	199.1	199.1	201.8 ± 1.4	202.1 ± 0.6	-	-	-
45	195.0	195.0	197.9 ± 1.2	197.7 ± 0.6	-	-	-
50	190.1	190.1	192.8 ± 0.9	192.9 ± 0.7	-	-	-
55	184.4	184.4	187.3 ± 0.9	187.2 ± 0.7	-	-	-
60	177.8	177.8	180.7 ± 0.8	180.5 ± 0.7	-	-	-
65	170.1	170.1	173.2 ± 0.6	173.3 ± 0.6	-	-	-
70	160.8	160.8	164.2 ± 0.7	162.7 ± 1.1	-	-	-
75	149.5	149.5	152.4 ± 0.7	152.4 ± 2.2	-	-	-
80	135.0	135.0	136.8 ± 1.3	137.2 ± 2.4	-	-	-
85	114.3	114.3	111.2 ± 3.3	112.4 ± 8.3	-	-	-
89	85.7	85.4	87.7 ± 9.9	106.1 ± 7.7	-	-	-
90	82.8	82.6	-	-	-	-	-

*For the latitude 20.25˚N. #For the latitude 26.25˚N.

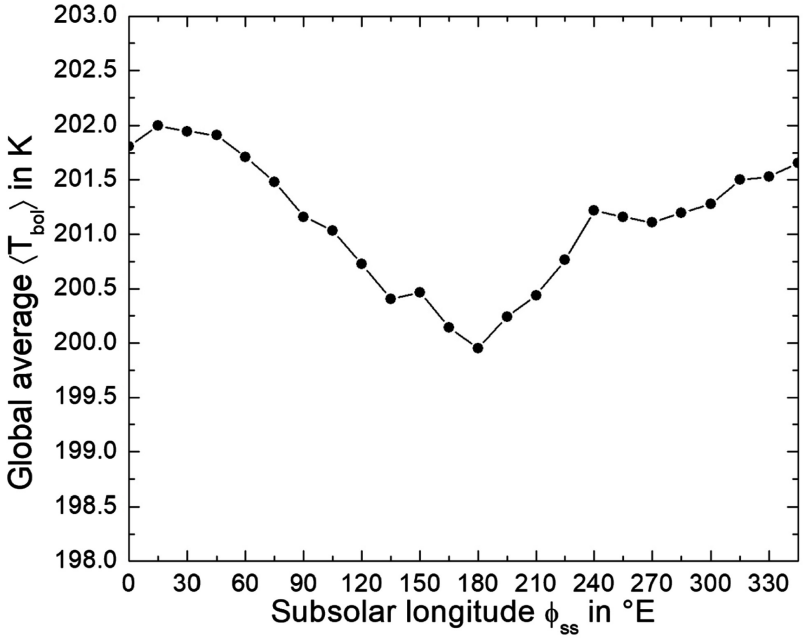

Figure 20. Globally averaged bolometric temperature, $\langle T_{bol} \rangle$, for all 24 DLRE datasets related to the subsolar longitude ϕ_{ss}.

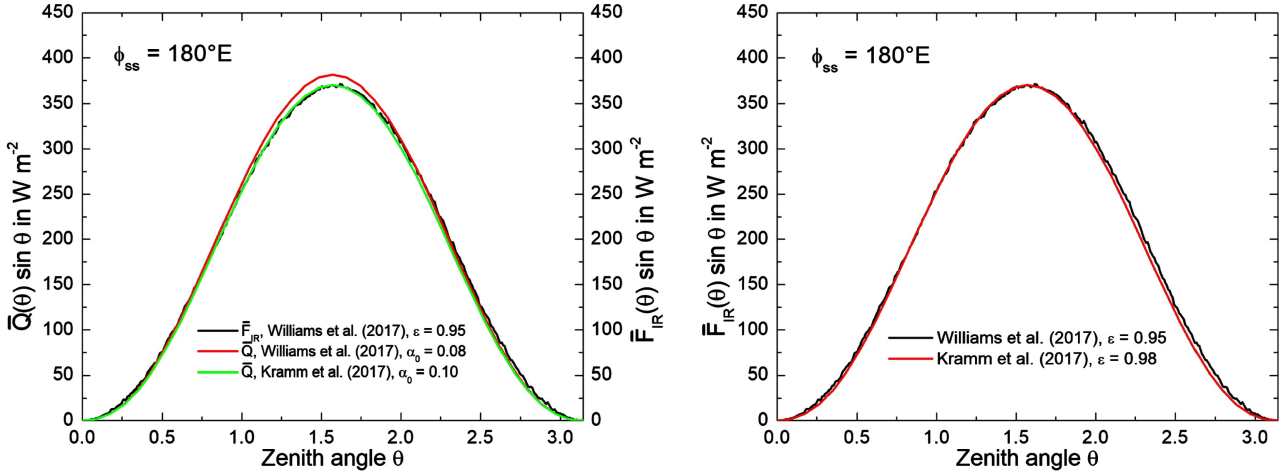

Figure 21. Meridional distributions of the zonal averages of the absorbed solar radiation, $\bar{Q}(\theta)$, and the emitted infrared radiation, $\bar{F}_{IR}(\theta)$, both weighted by $\sin\theta$ as required by Equation (1.2) for global averaging.

$T_{e,M} = \langle T_{bol}^4 \rangle^{1/4} = 271.0\,\mathrm{K} \pm 0.7\,\mathrm{K}$. **Figure 22** also shows the emission of infrared radiation calculated by applying the Stefan-Boltzmann power law to the globally averaged bolometric temperatures illustrated in **Figure 20**, *i.e.*,

$$\varepsilon\sigma\langle T_{bol} \rangle^4 < \langle \varepsilon\sigma T_{bol}^4 \rangle \tag{6.1}$$

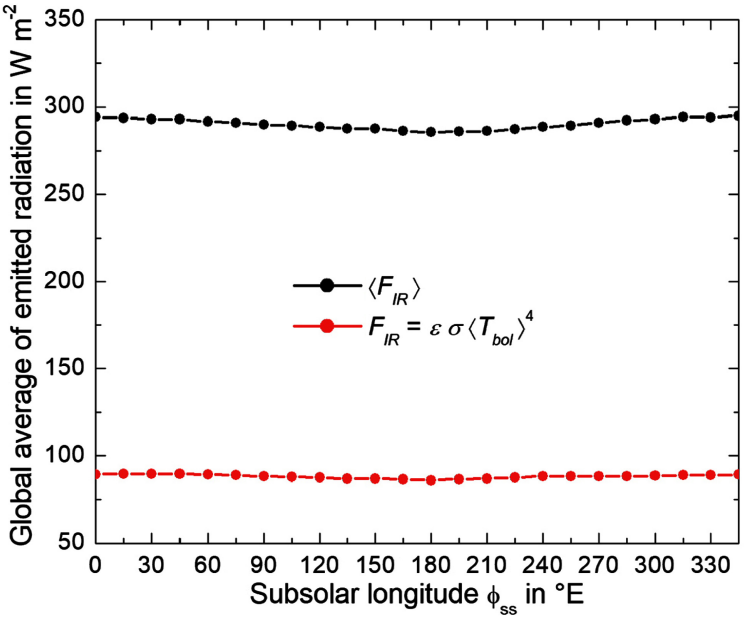

Figure 22. Globally averaged emitted infrared radiation $\left\langle \varepsilon\sigma T_{bol}^{4} \right\rangle$, derived from the 24 DLRE datasets of the bolometric temperature related to the subsolar longitude ϕ_{ss}. Also illustrated are the results provided by the inadequate application of the Stefan-Boltzmann law to the global mean of the bolometric temperature expressed by $\varepsilon\sigma\langle T_{bol}\rangle^{4}$.

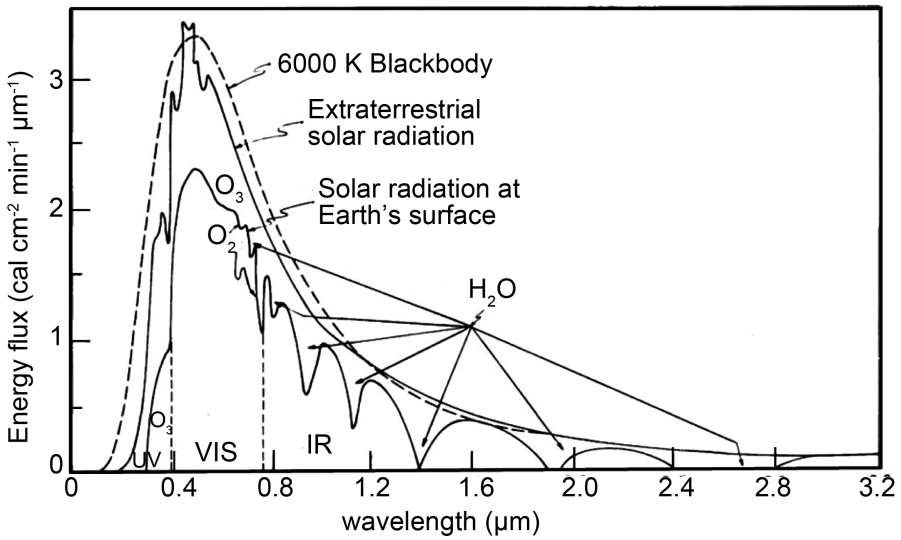

Figure 23. Spectral distribution of solar radiation at the TOA, and a typical distribution of that which reaches the Earth's surface, compared with the radiation emitted by a blackbody at a temperature of 6000 K (adopted from Coulson [110]).

Apparently, this kind of calculation is meritless. Therefore, it is time to acknowledge that the Stefan-Boltzmann power law must not be applied to globally averaged temperatures.

The DLRE data provide observational evidence that the concept of the effective radiation temperature must be discarded for planets and their natural satellites. In the case of stars, for which the concept of the

effective radiation temperature was derived, the condition of a uniformly distributed emittance may be crudely fulfilled, and the stars' emission spectra may be approximated by Planck's blackbody radiation function related to their effective radiation temperatures, as illustrated in **Figure 23** for our Sun. The condition of a uniform distribution of the emittance, however is, by far, not fulfilled in the case of planets and their natural satellites. In addition, their emission spectra vary with latitude and time. This fact is the reason why radiometers use different channels as illustrated by **Figure 15** and **Figure 16** to cover the wide range of surface temperatures. Since the maximum of the intensity of Planck's blackbody radiation function is proportional to the fifth power of the temperature [8, 86, 108, 109], averaging over the Planck functions for different temperatures is physically and mathematically awkward.

7. SUMMARY AND CONCLUSIONS

In our paper, we discussed the solar climate of the Moon and the distribution of its resulting surface temperature. Since the solar climate, when handled in its historical sense, would lead to a surface temperature of 0 K for the dark site of the Moon, it is essential to expand the concept of solar climate in such a way that such an artifact is generally excluded. Consequently, the local radiation balance (Equation (1.12)) must be replaced, at least, by a local energy flux budget (Equation (2.5)) to compute the related distribution of the surface temperature in a realistic manner. In this study, we used the multilayer-force-restore method by Kramm *et al.* [29] which applies the more advanced local energy budget expressed by Equation (2.3) to compute the distribution of the slab temperature, T_{slab} of the Moon. Predicted slab temperature is considered as the realistic surface temperature, and in a further step the global average of Moon's surface temperature. Their astrometric results derived from the data provided by JPL's planetary and lunar ephemeris DE430 underlined that the calculated solar insolation, required by their multilayer-force-restore method [29], meets the required accuracy criteria.

The numerical prediction was performed for 20 lunations starting May 24, 2009, 00:00 UT1 (Period I). Based on the astrometric results, we found for this period a mean heliocentric distance for the Moon of 1.00124279 AU and for the Earth of 1.00166376 AU. The corresponding mean geocentric distance of the Moon amounts to 384,792 km. Furthermore, we found that the synodic months deviate from their mean in a range of −5.7 h to 6.9 h and the draconic months depart from their mean by ±3.4 h. Whereas the anomalistic months depart from their mean in a range of −2.83 d to 0.97 d with the largest negative deviations occurring around the points of inflection in the curve that represents the departure of the synodic month from its mean. Moreover, based on the two successive passages of the Sun through the ascending node of the lunar equator plane during that Period I, we found that the time interval between them corresponds to 347.29 days, *i.e.*, it is slightly longer than the mean draconic year of 346.62 days.

Because the multilayer-force-restore method has to be spun up to equilibrium prior to analysis of the results, we analyzed only the results provided by it for the last 12 lunations starting January 15, 2010, 07:11 UT1 (Period II). As shown in our paper, the predicted slab temperatures follow the bolometric temperatures in an acceptable manner. Between 75˚N and 75˚S, most important to compute $\langle T_{slab} \rangle$ and $\langle T_{bol} \rangle$, the zonally averaged differences and the respective standard deviations are: 3.5 K ± 12.0 K for 75˚N 1.4 K ± 8.0 K for 60˚N, 0.9 K ± 6.5 K for 45˚N, 0.7 K ± 6.4 K for 30˚N, 0.4 K ± 6.3 K for 15˚N, 0.3 K ± 5.8 K for 0˚, 0.0 K ± 5.1 K for 15˚S, 0.1 K ± 5.8 K for 30˚S, 0.4 K ± 6.3 K for 45˚S, −0.4 K ± 8.1 K for 60˚S, and 0.2 K ± 10.2 K for 75˚S. Based on the observations performed at the landing site of the Apollo 15 mission, we showed that the occurrence of the two lunar eclipses has only a negligible effect on the zonal averages of the surface temperature if twelve lunations are considered.

The global averages of the bolometric temperature, $\langle T_{bol} \rangle$ for all 24 DLRE datasets related to the subsolar longitude ϕ_{ss} amount to $\langle T_{bol} \rangle = 201.1\,\mathrm{K} \pm 0.6\,\mathrm{K}$. Based on the globally averaged emitted infrared radiation of $\langle F_{IR} \rangle = 290.5\ \mathrm{W \cdot m^{-2}} \pm 3.0\ \mathrm{W \cdot m^{-2}}$ derived from these 24 DLRE datasets, the effective radiative temperature of the Moon is $T_{e,M} = \langle T_{bol}^4 \rangle^{1/4} = 271.0\,\mathrm{K} \pm 0.7\,\mathrm{K}$ so that $\langle T_{bol} \rangle \cong 0.742 T_{e,M}$. This means that in the case of the Moon, the effective radiation temperature is about 60 K higher than the glo-

bally averaged surface temperature.

Furthermore, our results obtained by means of the DLRE observations confirm Kramm *et al.* [29] who obtained for the Moon $\langle T_{slab} \rangle \cong 197.9$ K and $T_{e,M} = \langle T_{slab}^4(\theta,\varphi) \rangle^{1/4} \cong 266.4$ K resulting in $\langle T_{slab} \rangle \cong 0.743 T_{e,M}$. Our results also empirically confirm the temperature inequality (1.17) of Gerlich and Tscheuschner [53], *i.e.*, $\langle T_{bol} \rangle < \langle T_{bol}^4 \rangle^{1/4} = T_{e,M}$.

Obviously, the relationship between the global average of the surface temperature and the effective radiative temperature of a rocky celestial body differs by a factor that depends on the astronomical parameters, especially on the angular velocity of rotation. Kramm *et al.* [29], for instance, found for the solar climate of the 27.4 times faster rotating Earth $\langle T_{slab} \rangle \cong 0.828 T_{e,E}$. Consequently, the DLRE observations provide empirical evidence that in the case of rocky planets and their natural satellites, the globally averaged surface temperature is notably lower than their effective radiation temperature. Finally, based on the 24 DLRE datasets our study showed that applying the Stefan-Boltzmann power law to the globally averaged bolometric temperatures provides meritless results for rocky celestial bodies.

ACKNOWLEDGEMENTS

We would like to express our thanks to the JPL team around Drs. James G. Williams and William M. Folkner for making the planetary and lunar ephemeris DE 430 and the respective FORTRAN subroutines asc2eph, testeph, and PLEPH available for us, and to the anonymous reviewers for helpful comments and suggestions.

CONFLICTS OF INTEREST

The authors declare no conflicts of interest regarding the publication of this paper.

REFERENCES

1. Hann, J. (1883) Handbuch der Klimatologie. J. Engelhorn, Stuttgart.
2. Hann, J. and Ward, R.D.C. (1903) Handbook of Climatology. Macmillan, New York.
3. Bretagnon, P. (1974) Termes a longues periodes dans le systeme solaire. *Astronomy & Astrophysics*, **30**, 141-154.
4. Berger, A. (1978) Long-Term Variations of Daily Insolation and Quaternary Climatic Changes. *Journal of the Atmospheric Sciences*, **35**, 2362-2367. https://doi.org/10.1175/1520-0469(1978)035%3C2362:LTVODI%3E2.0.CO;2
5. Berger, A. (1988) Milankovitch Theory and Climate. *Reviews of Geophysics*, **26**, 624-657. https://doi.org/10.1029/RG026i004p00624
6. Lindzen, R.S. (1994) Climate Dynamics and Global Change. *Annual Review of Fluid Mechanics*, **26**, 353-378. https://doi.org/10.1146/annurev.fl.26.010194.002033
7. Monin, A.S. and Shishkov, Y.A. (2000) Climate as a Problem in Physics. *Uspekhi Fizicheskikh Nauk*, **170**, 419-445. https://doi.org/10.3367/UFNr.0170.200004d.0419
8. Liou, K.N. (2002) An Introduction to Atmospheric Radiation. 2nd Edition, Academic Press, San Diego.
9. Kramm, G. and Dlugi, R. (2011) Scrutinizing the Atmospheric Greenhouse Effect and Its Climatic Impact. *Natural Science*, **3**, 971-998. https://doi.org/10.4236/ns.2011.312124
10. Kramm, G. (2020) Kommentar zu WEBER (2019): Weitere Überlegungen zur hemisphärischen Herleitung einer globalen Durchschnittstemperatur. *DGG-Mitteilungen*, No. 2, 6-25.
11. Stefan, J. (1879) Über die Beziehung zwischen der Wärmestrahlung und der Temperatur. *Sitzungsberichte der Kaiserlichen Akademie der Wissenschaften in Wien*, **79**, 391-428.

12. Boltzmann, L. (1884) Ableitung des Stefan'schen Gesetzes, betreffend die Abhängigkeit der Wärmestrahlung von der Temperatur aus der electromagnetischen Lichttheorie. *Annalen der Physik*, **258**, 291-294. https://doi.org/10.1002/andp.18842580616
13. Kopp, G., Krivova, N., Wu, C.J. and Lean, J. (2016) The Impact of the Revised Sunspot Record on Solar Irradiance Reconstructions. *Solar Physics*, **291**, 2951-2965. https://doi.org/10.1007/s11207-016-0853-x
14. Kopp, G. and Lean, J.L. (2011) A New, Lower Value of Total Solar Irradiance: Evidence and Climate Significance. *Geophysical Research Letters*, **38**, Article ID: L01706. https://doi.org/10.1029/2010GL045777
15. Raschke, E., Vonder Haar, T.H., Bandeen, W.R. and Pasternak, M. (1973) The Annual Radiation Balance of the Earth-Atmosphere System during 1969-1970 from Nimbus III Measurements. *Journal of the Atmospheric Sciences*, **30**, 341-364. https://doi.org/10.1175/1520-0469(1973)030%3C0341:TARBOT%3E2.0.CO;2
16. Kopp, G. (2021) Science Highlights and Final Updates from 17 Years of Total Solar Irradiance Measurements from the *SOlar Radiation and Climate Experiment*/*Total Irradiance Monitor* (SORCE/TIM). *Solar Physics*, **296**, Article No. 133. https://doi.org/10.1007/s11207-021-01853-x
17. Schoch, W. (1856) Über die Darstellung der mittlern Jahrestemperatur eines Ortes als Function seiner geographischen Länge und Breite. University of Zurich, Zurich.
18. Ferrel, W. (1877) Meteorological Researches. U.S. Government Publishing Office, Washington DC.
19. Spitaler, R. (1886) Die Wärmeverteilung auf der Erdoberfläche. In: *Denkschriften der mathem.-naturwiss. Klasse der Kaiserl.* Akademie der Wissenschaften in Wien, Vienna, 1-20.
20. Hann, J. (1897) Handbuch der Klimatologie. Englehorn Stuttgart, Germany.
21. von Bezold, W. (1901) Über klimatologische Mittelwerthe für ganze Breitenkreise. In: *Sitzungsberichte der Königlich Preussischen Akademie der Wissenschaften zu Berlin*, Deutsche Akademie der Wissenschaften zu Berlin, Berlin, 1330-1343. https://books.google.com/books?id=JdcAAAAAYAAJ
22. Börnstein, R. (1913) *Leitfaden der Wetterkunde*. F. Vieweg und Sohn.
23. Fortak, H. (1971) Meteorologie. Deutsche Buch-Gemeinschaft, Berlin/Darmstadt/Wien.
24. Hansen, J., Johnson, D., Lacis, A., Lebedeff, S., Lee, P., Rind, D. and Russell, G. (1981) Climate Impact of Increasing Atmospheric Carbon-Dioxide. *Science*, **213**, 957-966. https://doi.org/10.1126/science.213.4511.957
25. Ramanathan, V., Callis, L., Cess, R., Hansen, J., Isaksen, I., Kuhn, W., Lacis, A., Luther, F., Mahlman, J., Reck, R. and Schlesinger, M. (1987) Climate-Chemical Interactions and Effects of Changing Atmospheric Trace Gases. *Reviews of Geophysics*, **25**, 1441-1482. https://doi.org/10.1029/RG025i007p01441
26. Kramm, G., Dlugi, R., Berger, M. and Mölders, N. (2020) Meridional Distributions of Historical Zonal Averages and Their Use to Quantify the Global and Spheroidal Mean Near-Surface Temperature of the Terrestrial Atmosphere. *Natural Science*, **12**, 80-124. https://doi.org/10.4236/ns.2020.123012
27. Kramm, G., Dlugi, R. and Zelger, M. (2009) Comments on the "Proof of the Atmospheric Greenhouse Effect" by Arthur P. Smith. http://arxiv.org/abs/0904.2767v3
28. Hantel, M. and Haimberger, L. (2016) Grundkurs Klima. Springer-Verlag Berlin, Heidelberg. https://doi.org/10.1007/978-3-662-48193-6
29. Kramm, G., Dlugi, R. and Mölders, N. (2017) Using Earth's Moon as a Testbed for Quantifying the Effect of the Terrestrial Atmosphere. *Natural Science*, **9**, 251-288. https://doi.org/10.4236/ns.2017.98026
30. Peixoto, J.P. and Oort, A.H. (1984) Physics of Climate. *Reviews of Modern Physics*, **56**, 365-429. https://doi.org/10.1103/RevModPhys.56.365
31. Peixoto, J.P. and Oort, A.H. (1992) Physics of Climate. American Institute of Physics, New York.
32. Wiin-Nielsen, A. and Chen, T.C. (1993) Fundamentals of Atmospheric Energetics. Oxford University Press,

Oxford.

33. Schack, A. (1972) Der EinfluB des Kohlendioxid-Gehaltes der Luft auf das Klima dar Welt. *Physikalische Blätter*, **28**, 26-28. https://doi.org/10.1002/phbl.19720280106
34. Budyko, M.I. (1977) Climatic Changes. Vol. 10, American Geophysical Union, Washington DC. https://doi.org/10.1029/SP010
35. Emden, R. (1913) Über Strahlungsgleichgewicht und atmosphärische Strahlung. In: *Sitzungsberichte der mathematisch-physikalischen Klasse*, K. B. Akademie der Wissenschaften, München, 55-142.
36. Defant, A. and Obst, E. (1923) Lufthulle und Klima. F. Deuticke, Leipzig, Wien.
37. Lenard, P. (1936) *Deutsche Physik. Zweiter Band: Akustik und Wärmelehre*. J.F. Lehmanns Verlag, München.
38. Möller, F. (1964) Optics of the Lower Atmosphere. *Applied Optics*, **3**, 157-166. https://doi.org/10.1364/AO.3.000157
39. Williams, J.P., Paige, D.A., Greenhagen, B.T. and Sefton-Nash, E. (2017) The Global Surface Temperatures of the Moon as Measured by the Diviner Lunar Radiometer Experiment. *Icarus*, **283**, 300-325. https://doi.org/10.1016/j.icarus.2016.08.012
40. Abbot, C.G. (1911) The Sun's Energy-Spectrum and Temperature. *The Astrophysical Journal*, **34**, 197. https://doi.org/10.1086/141881
41. Chandrasekhar, S. (1960) Radiative Transfer. Dover Publications, New York.
42. Unsöld, A. (1968) Physik der Sternatmosphären, mit besonder Berücksichtigung der Sonne. Springer-Verlag, Berlin, Heidelber, New York.
43. Haltiner, G.J. and Martin, F.L. (1957) Dynamical and Physical Meteorology. McGraw-Hill Book Company, New York/Toronto/London.
44. Möller, F. (1973) Einführung in die Meteorologie. Bibliographisches Institut, Mannheim/Wien/Zürich.
45. Emilio, M., Kuhn, J.R., Bush, R.I. and Scholl, I.F. (2012) Measuring the Solar Radius from Space during the 2003 and 2006 Mercury Transits. *The Astrophysical Journal*, **750**, 135. https://doi.org/10.1088/0004-637X/750/2/135
46. Petty, G.W. (2004) A First Course in Atmospheric Radiation. Sundog Publishing, Madison.
47. Bohren, C.F. and Clothiaux, E.E. (2006) Fundamentals of Atmospheric Radiation. Wiley-VCH, Berlin. https://doi.org/10.1002/9783527618620
48. Butler, J.J., Johnson, B.C., Rice, J.P., Shirley, E.L. and Barnes, R.A. (2008) Sources of Differences in On-Orbital Total Solar Irradiance Measurements and Description of a Proposed Laboratory Intercomparison. *Journal of Research of the National Institute of Standards and Technology*, **113**, 187-203. https://doi.org/10.6028/jres.113.014
49. Lean, J.L. (2010) Cycles and Trends in Solar Irradiance and Climate. *WIREs Climate Change*, **1**, 111-122. https://doi.org/10.1002/wcc.18
50. Kopp, G., Fehlmann, A., Finsterle, W., Harber, D., Heuerman, K. and Willson, R. (2012) Total Solar Irradiance Data Record Accuracy and Consistency Improvements. *Metrologia*, **49**, S29-S33. https://doi.org/10.1088/0026-1394/49/2/S29
51. Rathbun, J.A., Spencer, J.R., Tamppari, L.K., Martin, T.Z., Barnard, L. and Travis, L.D. (2004) Mapping of Io's Thermal Radiation by the Galileo Photopolarimeter-Radiometer (PPR) Instrument. *Icarus*, **169**, 127-139. https://doi.org/10.1016/j.icarus.2003.12.021
52. Joseph, C. and Michael, S. (2011) The Occurrence Rate of Earth Analog Planets Orbiting Sun-Like Stars. *The Astrophysical Journal*, **738**, Article No. 151. https://doi.org/10.1088/0004-637X/738/2/151

53. Gerlich, G. and Tscheuschner, R.D. (2009) Falsification of the Atmospheric CO_2 Greenhouse Effects within the Frame of Physics. *International Journal of Modern Physics B*, **23**, 275-364. https://doi.org/10.1142/S021797920904984X

54. Hölder, O. (1889) Über einen Mittelwertsatz. Nachrichten von der Gesellschaft der Wissenschaften zu Göttingen, Göttingen, 38-47.

55. Hardy, G.H., Littlewood, J.E. and Pólya, G. (1934) Inequalities. Cambridge University Press, Cambridge.

56. Keihm, S.J. (1984) Interpretation of the Lunar Microwave Brightness Temperature Spectrum: Feasibility of Orbital Heat Flow Mapping. *Icarus*, **60**, 568-589. https://doi.org/10.1016/0019-1035(84)90165-9

57. Paige, D.A., Foote, M.C., Greenhagen, B.T., Schofield, J.T., Calcutt, S., Vasavada, A.R., Preston, D.J., Taylor, F.W., Allen, C.C., Snook, K.J., Jakosky, B.M., Murray, B.C., Soderblom, L.A., Jau, B., Loring, S., Bulharowski, J., Bowles, N.E., Thomas, I.R., Sullivan, M.T., Avis, C., De Jong, E.M., Hartford, W. and McCleese, D.J. (2010) The Lunar Reconnaissance Orbiter Diviner Lunar Radiometer Experiment. *Space Science Reviews*, **150**, 125-160. https://doi.org/10.1007/s11214-009-9529-2

58. Vasavada, A.R., Bandfield, J.L., Greenhagen, B.T., Hayne, P.O., Siegler, M.A., Williams, J.-P. and Paige, D.A. (2012) Lunar Equatorial Surface Temperatures and Regolith Properties from the Diviner Lunar Radiometer Experiment. *Journal of Geophysical Research*, **117**, E00H18. https://doi.org/10.1029/2011JE003987

59. Chin, G., Brylow, S., Foote, M., *et al.* (2007) Lunar Reconnaissance Orbiter Overview: The Instrument Suite and Mission. *Space Science Reviews*, **129**, 391-419. https://doi.org/10.1007/s11214-007-9153-y

60. Tooley, C., Houghton, M.B., Saylor, R.S., *et al.* (2010) Lunar Reconnaissance Orbiter Mission and Spacecraft Design. *Space Science Reviews*, **150**, 23-62.

61. Vondrak, R., Keller, J., Chin, G. and Garvin, J. (2010) Lunar Reconnaissance Orbiter (LRO): Observations for Lunar Exploration and Science. *Space Science Reviews*, **150**, 7-22. https://doi.org/10.1007/s11214-010-9631-5

62. Wesselink, A.F. (1948) Heat Conductivity and Nature of the Lunar Surface Material. *Bulletin of the Astronomical Institutes of the Netherlands*, **10**, 351-363.

63. Jaeger, J.C. (1953) The Surface Temperature of the Moon. *Australian Journal of Physics*, **6**, 10-21.

64. Cremers, C.J., Birkebak, R.C. and White, J.E. (1971) Lunar Surface Temperature at Tranquility Base. *AIAA Journal*, **9**, 1899-1903. https://doi.org/10.2514/3.50000

65. Mitchell, D.L. and de Pater, I. (1994) Microwave Imaging of Mercury's Thermal Emission at Wavelengths from 0.3 to 20.5 cm. *Icarus*, **110**, 2-32. https://doi.org/10.1006/icar.1994.1105

66. Vasavada, A.R., Paige, D.A. and Wood, S.E. (1999) Near-Surface Temperatures on Mercury and the Moon and the Stability of Polar Ice Deposits. *Icarus*, **141**, 179-193. https://doi.org/10.1006/icar.1999.6175

67. Bauch, K.E., Hiesinger, H., Helbert, J., Robinson, M.S. and Scholten, F. (2014) Estimation of Lunar Surface Temperatures and Thermophysical Properties: Test of a Thermal Model in Preparation of the MERTIS Experiment Onboard BepiColombo. *Planetary and Space Science*, **101**, 27-36. https://doi.org/10.1016/j.pss.2014.06.004

68. Bauch, K.E., Hiesinger, H., Greenhagen, B.T. and Helbert, J. (2021) Estimation of Surface Temperatures on Mercury in Preparation of the MERTIS Experiment Onboard BepiColombo. *Icarus*, **354**, Article ID: 114083. https://doi.org/10.1016/j.icarus.2020.114083

69. Hu, G.-p., Zheng, Y.-C., Xu, A.-A. and Tang, Z.-S. (2015) Lunar Surface Temperature of Global Moon: Preparation of Database with Topographic and Albedo Effects. *IEEE Geoscience and Remote Sensing Letters*, **13**, 110-114. https://doi.org/10.1109/LGRS.2015.2499305

70. Soter, S. and Ulrichs, J. (1967) Rotation and Heating of the Planet Mercury. *Nature*, **214**, 1315-1314. https://doi.org/10.1038/2141315a0

71. Morrison, D. (1970) Thermophysics of the Planet Mercury. *Space Science Reviews*, **11**, 271-307.

https://doi.org/10.1007/BF00241524

72. Keihm, S.J., Peters, K., Langseth, M.G. and Chute, J.L. (1973) Apollo 15 Measurement of Lunar Surface Brightness Temperatures Thermal Conductivity of the Upper 1 1/2 Meters of Regolith. *Earth and Planetary Science Letters*, **19**, 337-351. https://doi.org/10.1016/0012-821X(73)90084-8

73. Keihm, S.J. and Langseth, M.G. (1973) Surface Brightness Temperatures at the Apollo 17 Heat Flow Site—Thermal Conductivity of the Upper 15 cm of Regolith. *Proceedings of the* 4*th Lunar Science Conference*, Houston, 5-8 March 1973, 2503-2513.

74. Hiesinger, H., Helbert, J., Alemanno, G., Bauch, K.E., D'Amore, M., Maturilli, A., Morlok, A., Reitze, M.P., Stangarone, C., Stojic, A.N., Varatharajan, I., Weber, I. and the MERTIS Co-I Team (2020) Studying the Composition and Mineralogy of the Hermean Surface with the Mercury Radiometer and Thermal Infrared Spectrometer (MERTIS) for the BepiColombo Mission: An Update. *Space Science Reviews*, **216**, Article No. 110. https://doi.org/10.1007/s11214-020-00732-4

75. Kramm, G., Beier, N., Foken, T., Muller, H., Schroder, P. and Seiler, W. (1996) A SVAT Scheme for NO, NO_2, and O_3—Model Description and Test results. *Meteorology and Atmospheric Physics*, **61**, 89-106. https://doi.org/10.1007/BF01029714

76. Mölders, N., Haferkorn, U., Döring, J. and Kramm, G. (2003) Long-Term Investigations on the Water Budget Quantities Predicted by the Hydro-Thermodynamic Soil Vegetation Scheme (HTSVS)—Part I: Description of the Model and Impact of Long-Wave Radiation, Roots, Snow, and Soil Frost. *Meteorology and Atmospheric Physics*, **84**, 115-135. https://doi.org/10.1007/s00703-002-0578-2

77. Hagermann, A. (2005) Planetary Heat Flow Measurements. *Philosophical Transactions of the Royal Society A*, **363**, 2777-2791. https://doi.org/10.1098/rsta.2005.1664

78. Hemingway, B.S., Robie, R.A. and Wilson, W.H. (1973) Specific Heats of Lunar Soils, Basalt, and Breccias from the Apollo 14, 15, and 16 Landing Sites, between 90 and 350 ˚K. *Proceedings of the* 4*th Lunar Science Conference*, Houston, 5-8 March 1973, 2481-2487.

79. Wechsler, A.E., Glaser, P.E., Little, A.D. (1972) Thermal Properties of Granulated Materials. In: *Thermal Characteristics of the Moon*, American Institute of Aeronautics and Astronautics, Reston, 215-241. https://doi.org/10.2514/5.9781600865022.0215.0241

80. Meech, L.W. (1857) On the Relative Intensity of the Heat and Light of the Sun upon Different Latitudes of the Earth. Vol. 9, Smithsonian Contributions to Knowledge, Washington DC.

81. Wiener, C. (1877) Ueber die Stärke der Bestrahlung der Erde durch die Sonne in den verschiedenen Breiten und Jahreszeiten. *Zeitschrift fuer Mathematik und Physik*, **22**, 341-368.

82. Wiener, C. (1879) Ueber die Stärke der Bestrahlung der Erde durch die Sonne in den verschiedenen Breiten und Jahreszeiten. *Meteorologische Zeitschrift*, 113-130.

83. Milankovitch, M. (1941) Kanon der Erdbestrahlungen und seine Anwendung auf das Eiszeitenproblem. Section of Mathematical and Natural Sciences, Vol. 33, Royal Serbian Academy, Belgrade.

84. Kondratyev, K.Y. (1969) Radiation in the Atmosphere. Academic Press, New York/London.

85. Milankovitch, M. (1920) Théorie mathématique des phénomènes thermiques produits par la radiation solaire. Gauthier-Villars, Paris.

86. Mölders, N. and Kramm, G. (2014) Lectures in Meteorology. Springer International Publishing, Cham. https://doi.org/10.1007/978-3-319-02144-7

87. Iqbal, M. (1983) An Introduction to Solar Radiation. Academic Press, Canada.

88. Folkner, W.M., Williams, J.G., Boggs, D.H., Park, R.S. and Kuchynka, P. (2014) The Planetary and Lunar Ephemerides DE430 and DE431. IPN Progress Report, Jet Propulsion Laboratory, California Institute of Tech-

nology, Pasadena, 81.

89. Park, R.S., Folkner, W.M., Williams, J.G. and Boggs, D.H. (2021) The JPL Planetary and Lunar Ephemerides DE440 and DE441. *The Astronomical Journal*, **161**, Article No. 105. https://doi.org/10.3847/1538-3881/abd414
90. Taylor, D.B., Bell, S.A., Hilton, J.L., Sinclair, A.T. (2010) Computation of the Quantities Describing the Lunar Librations in the Astronomical Almanac. HM Nautical Almanac Office, UK Hydrographic Office, Taunton.
91. Newhall, X.X. and Williams, J.G. (1996) Estimation of the Lunar Physical Librations. *Celestial Mechanics and Dynamical Astronomy*, **66**, 21-30. https://doi.org/10.1007/BF00048820
92. Simon, J.L., Bretagnon, P., Chapront, J., Chapront-Touze, M., Francou, G., Laskar, J. (1994) Numerical Expressions for Precession Formulae and Mean Elements for the Moon and the Planets. *Astronomy and Astrophysics*, **282**, 663-683.
93. Pielke, R.A. (2002) Mesoscale Meteorological Modeling. Academic Press, San Diego/San Francisco/New York/Boston/London/Sydney/Tokyo, 676.
94. Espenak, F. and Meeus, J. (2009) Five Millennium Catalog of Solar Eclipses: −1999 to +3000 (2000 BCE to 3000 CE)—Revised. National Aeronautics and Space Administration (NASA), Greenbelt.
95. Smart, W.M. (1949) Text-Book on Spherical Astronomy. Cambridge University Press, Cambridge.
96. Seidelmann, P.K.E. (1992) Explanatory Supplement to the Astronomical Almanac. University Science Books, Mill Valley.
97. Moulton, F.R. (1918) An Introduction to Astronomy. The MacMillan Company, New York
98. Allen, C.W. (1976) Astrophysical Quantities. University of London. The Athlone Press, London.
99. Unsöld, A. (1967) Der neue Kosmos. Springer-Verlag, Berlin/Heidelberg/New York. https://doi.org/10.1007/978-3-662-30219-4
100. Espenak, F. and Meeus, J. (2009) Five Millennium Canon of Lunar Eclipses: −1999 to +3000 (2000 BCE to 3000 CE). National Aeronautics and Space Administration (NASA), Greenbelt.
101. Roncoli, R.B. (2005) Lunar Constants and Models Document. Jet Propulsion Laboratory, California Institute of Technology, Pasadena, 68.
102. Barbieri, C. (2017) Fundamentals of Astronomy. CRC Press, Boca Raton. https://doi.org/10.1201/9781315275994
103. Planck, M. (1901) Ueber das Gesetz der Energieverteilung im Normalspectrum. *Annalen der Physik*, **309**, 553-563. https://doi.org/10.1002/andp.19013090310
104. Paige, D.A., Siegler, M.A., Zhang, J.A., Hayne, P.O., Foote, E.J., Bennett, K.A., Vasavada, A.R., Greenhagen, B.T., Schofield, J.T., McCleese, D.J., Foote, M.C., DeJong, E., Bills, B.G., Hartford, W., Murray, B.C., Allen, C.C., Snook, K., Soderblom, L.A., Calcutt, S., Taylor, F.W., Bowles, N.E., Bandfield, J.L., Elphic, R., Ghent, R., Glotch, T.D., Wyatt, M.B. and Lucey, P.G. (2010) Diviner Lunar Radiometer Observations of Cold Traps in the Moon's South Polar Region. *Science*, **330**, 479-482. https://doi.org/10.1126/science.1187726
105. Greenhagen, B.T. (2009) Thermal Emission Remote Sensing of the Moon: Design and Development of Diviner Lunar Radiometer Compositional Capabilities. Ph.D. Thesis, University of California, Los Angeles.
106. Sullivan, M.T., Paige, D.A., Arvidson, R.E. and Grayzeck, E. (2013) Lunar Reconnaissance Orbiter Diviner Lunar Radiometer Experiment: Reduced Data Record and Derived Products Software Interface Specification. PDS Geosciences Node, Washington University, St. Louis.
107. Williams, J.P., Sefton-Nash, E. and Paige, D.A. (2016) The Temperatures of Giordano Bruno Crater Observed by the Diviner Lunar Radiometer Experiment: Application of an Effective Field of View Model for a Point-Based Data Set. *Icarus*, **273**, 205-213. https://doi.org/10.1016/j.icarus.2015.10.034

108. Planck, M. (1913) Vorlesungen über die Theorie der Wärmestrahlung. Verlag Johann Ambrosius Barth, Leipzig.
109. Planck, M. (1914) The Theory of Heat Radiation. P. Blakiston's Son & Co, Philadelphia, 225.
110. Coulson, K.L. (1975) Solar and Terrestrial Radiation. Academic Press, New York/San Francisco/London.